

# The Keck-HGCA Pilot Survey II: Direct Imaging Discovery of HD 63754 B, a $\sim$ 20 au Massive Companion Near the Hydrogen Burning Limit

Yiting Li<sup>1,8\*</sup>, Timothy D. Brandt<sup>1</sup>, Kyle Franson<sup>2</sup>, Qier An<sup>1</sup>, Taylor Tobin<sup>8</sup>, Thayne Currie<sup>7</sup>, Minghan Chen<sup>1</sup>, Lanxuan Wang<sup>1</sup>, Trent J. Dupuy<sup>3</sup>, Rachel Bowens-Rubin<sup>4</sup>, Maïssa Salama<sup>4</sup>, Briley L. Lewis<sup>5</sup>, Aidan Gibbs<sup>5</sup>, Brendan P. Bowler<sup>2</sup>, Rebecca Jensen-Clem<sup>4</sup>, Jacqueline Faherty<sup>6</sup>, Michael P. Fitzgerald<sup>5</sup>,

Benjamin A. Mazin<sup>1</sup>

<sup>1</sup>Department of Physics, University of California, Santa Barbara, Santa Barbara, CA 93106, USA

<sup>2</sup>Department of Astronomy, The University of Texas at Austin, Austin, TX 78712, USA

<sup>3</sup>Institute for Astronomy, University of Edinburgh, Royal Observatory, Blackford Hill, Edinburgh, EH9 3HJ, UK

<sup>4</sup>Astronomy & Astrophysics Department, University of California, Santa Cruz, CA 95064, USA

<sup>5</sup>Department of Physics and Astronomy, University of California, Los Angeles, 475 Portola Plaza, Los Angeles, CA 90025

<sup>6</sup>American Museum of Natural History, New York, NY, USA

<sup>7</sup>The University of Texas at San Antonio, San Antonio, TX 78249

<sup>8</sup>Department of Astronomy, University of Michigan, Ann Arbor, MI 48109

Accepted XXX. Received YYY; in original form ZZZ

## ABSTRACT

We present the joint astrometric and direct imaging discovery, mass measurement, and orbital analysis of HD 63754 B (HIP 38216 B), a companion near the stellar-substellar boundary orbiting  $\sim$ 20 AU from its Sun-like host. HD 63754 was observed in our ongoing high-contrast imaging survey targeting stars with significant proper-motion accelerations between *Hipparcos* and *Gaia* consistent with wide-separation substellar companions. We utilized archival HIRES and HARPS radial velocity (RV) data, together with the host star's astrometric acceleration extracted from the *Hipparcos–Gaia* Catalog of Accelerations (HGCA), to predict the location of the candidate companion around HD 63754 A. We subsequently imaged HD 63754 B at its predicted location using the Near Infrared Camera 2 (NIRC2) in the  $L'$  band at the W. M. Keck Observatory. We then jointly modeled the orbit of HD 63754 B with RVs, *Hipparcos–Gaia* accelerations, and our new relative astrometry, measuring a dynamical mass of  $81.9^{+6.4}_{-5.8} M_{\text{Jup}}$ , an eccentricity of  $0.260^{+0.065}_{-0.059}$ , and a nearly face-on inclination of  $174.81^{+0.48}_{-0.50}$ . For HD 63754 B, we obtain an  $L'$  band absolute magnitude of  $L' = 11.39 \pm 0.06$  mag, from which we infer a bolometric luminosity of  $\log(L_{\text{bol}}/L_{\odot}) = -4.55 \pm 0.08$  dex using a comparison sample of L and T dwarfs with measured luminosities. Although uncertainties linger in age and dynamical mass estimates, our analysis points toward HD 63754 B's identity as a brown dwarf on the L/T transition rather than a low-mass star, indicated by its inferred bolometric luminosity and model-estimated effective temperature. Future RV, spectroscopic, and astrometric data such as those from JWST and Gaia DR4 will clarify HD 63754 B's mass, and enable spectral typing and atmospheric characterization.

Key words: methods: data analysis – techniques: high angular resolution – techniques: image processing – astrometry.

## 1 INTRODUCTION

Brown dwarfs are distinct from stars in that they do not have enough mass to sustain hydrogen fusion in their cores to counteract gravitational collapse. Instead, as they evolve, they are supported first by thermal pressure from a combination of deuterium burning and gravitational contraction, and ultimately by electron degeneracy pressure (Henriksen 1986; Chabrier et al. 2005; McKee & Ostriker 2007; André et al. 2009; Dobbs 2013; Schneider et al. 2015; Forbes & Loeb 2019; Nony et al. 2023). As a result of heat loss, they continuously cool across the L, T, Y spectrum and emit their light in the thermal infrared (Lunine et al. 1986). Brown dwarfs manifest temperatures lower than the coolest stars, occupying a range of surface temperatures, spanning 3000 K for the hottest L dwarfs (Kirkpatrick et al. 2000; Filippazzo et al. 2015) to a frosty 250 K for the coolest Y

dwarfs (Lodders & Fegley 2002; Beichman et al. 2013). However, recent discoveries, such as an 8000 K irradiated-Jupiter-analogue brown dwarf orbiting a hot white dwarf (Hallakoun et al. 2023), continue to challenge our understanding of the rich tapestry of brown dwarf diversity.

The mechanisms governing brown dwarf formation are still not fully understood, with several proposed channels (Whitworth 2018), including turbulent fragmentation (Padoan & Nordlund 2002, 2004), fragmentation within filaments and discs (Peretto et al. 2013; Balfour et al. 2015), dynamical ejection of protostellar embryos (Reipurth & Clarke 2001), and photoerosion (Hester et al. 1996). Observations are crucially needed to assess their relative importance. Substellar evolutionary models incorporating synthetic spectra, nongray atmosphere models, dust formation, and opacity have been developed to explain brown dwarfs' behavior in optical and infrared color-magnitude dia-

grams (Chabrier et al. 2000). These evolutionary models increasingly emphasize the impact of dynamic processes on internal structure and methane absorption in the atmosphere, which affects atmospheric opacity, as effective temperatures and radii decrease in brown dwarf evolution. According to the majority of evolutionary models that distinguish between stars and brown dwarfs by their physical attributes and internal chemical processes (Leggett et al. 1998; Levine et al. 2006; Allard et al. 2012; Gonzales 2020), the substellar-stellar boundary occurs near  $75 M_{\text{Jup}}$  (Dieterich et al. 2014; Pinochet 2019). However, Chabrier et al. (2023) recently incorporated a new Equation Of State (EOS) for dense hydrogen-helium mixtures to model the evolution of brown dwarfs and very low-mass stars, and found improved agreement with observationally determined brown dwarf masses. They report a slight increase in the hydrogen-burning minimum mass from the  $75 M_{\text{Jup}}$  by Dieterich et al. (2014) to  $78.5 M_{\text{Jup}}$ . Furthermore, statistical studies on the eccentricity and obliquity of directly imaged substellar companions around cool stars have revealed a common occurrence of spin misalignments, particularly favored by stars hosting brown dwarfs over giant planets (Bowler et al. 2020, 2023). (Bowler et al. 2020, 2023). These findings present promising opportunities for testing distinctions between brown dwarf and giant planet formation mechanisms.

Empirical observations of the diverse substellar population anchor our physical understanding. Brown dwarfs with observationally constrained masses, ages, and luminosities independent of models offer a means to establish benchmarks for calibrating and testing evolutionary models (Liu et al. 2002; Dupuy et al. 2009; Crepp & Johnson 2014; Crepp et al. 2014; Dupuy & Liu 2017; Dupuy et al. 2019; Franson et al. 2023). As an example, using very precise dynamical masses in the  $\varepsilon$  Indi BC system, Chen et al. (2022) found better agreement with evolutionary models that had slowed cooling rate near the L/T transition due to clouds and opacity effects in the atmospheres of brown dwarfs.

The high-contrast imaging technique has emerged as a potent method for detecting exoplanets, providing spatially resolved observations of brown dwarfs. However, first-generation direct imaging searches, which adopt a blind approach by targeting every young star, have yielded low detection rates (Bowler 2016; Nielsen et al. 2019). In recent years, attention has shifted towards targeted searches that focus on stars exhibiting stellar reflex motion, resulting in enhanced survey outcomes. Both radial velocity and astrometry techniques probe the reflex motion of stars in orthogonal directions. Radial velocity trends have been used to identify direct imaging follow-up companions (Crepp et al. 2014; Rickman et al. 2019), while astrometry trends as a target selection tool is a novel method that has been demonstrated to be effective by several surveys (Currie et al. 2023; Franson et al. 2023). The Hipparcos-Gaia Catalog of Accelerations (HGCA) (Brandt et al. 2021c) offers absolute astrometry for about 115,000 nearby stars, including those with clear evidence of massive, unseen companions. HGCA-derived accelerations can provide dynamical masses of imaged exoplanets and low-mass brown dwarfs independently of luminosity evolution models and stellar age uncertainties (Brandt et al. 2019; Dupuy et al. 2019).

In this paper, we report the discovery of a massive companion close to the hydrogen burning limit, at a separation of  $0.^{\circ}48$  from the Sun-like star HD 63754 A. The discovery of this companion was achieved within an ongoing survey concentrated on detecting substellar companions orbiting accelerating stars. The observations utilized infrared imaging through the NIRC2 instrument at Keck and the CHARIS integral field spectrograph at SCExAO/Subaru in Hawaii. This builds on our previous success in the survey, which yielded the discovery of a massive brown dwarf, HD 176535 B,

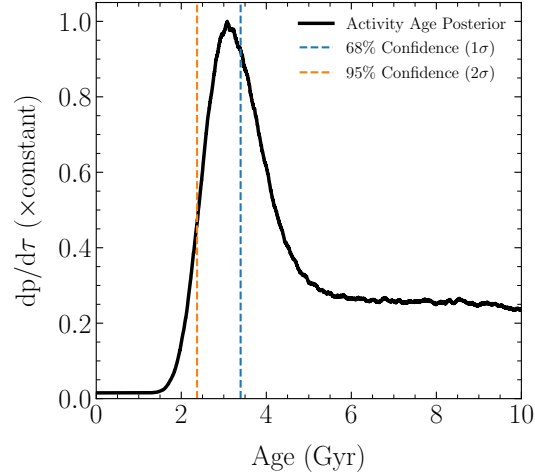


**Figure 1.** The normalized age probability posteriors of HD 63754 A using the Bayesian activity-age dating technique developed by Brandt et al. (2014). Given that the upper limit of the age is unconstrained, one-sided quantiles were calculated by integrating the area under the cumulative density function up to the 68% and 95% confidence levels, corresponding to the  $1\sigma$  and  $2\sigma$  confidence intervals, respectively. The age of HD 63754 A is estimated to be  $> 3.4$  Gyr at a 68% confidence level (blue dashed line), and  $> 2.4$  Gyr at a 95% confidence level (orange dashed line).

around a K-type star (Li et al. 2023). We present the dynamical mass determinations and orbital constraints for HD 63754 B using a combination of radial velocity, relative astrometry from direct imaging, and Hipparcos-Gaia DR3 accelerations. In Section 2, we discuss the stellar properties of the host star HD 63754 A. Following that, we describe the prediction of the companion for our survey program in Section 3. We present our observation and direct imaging discovery in Section 4. We discuss the modelings of the evolutionary properties and orbit of HD 63754 B in Section 5 and Section 6, and conclude in Section 7.

## 2 SYSTEM PROPERTIES

HD 63754 A (HIP 38216 A; HR 3048 A) is a bright ( $V \approx 6.98$  mag; ESA 1997), main-sequence star of spectral type G0V (Soubiran et al. 2018) located at a distance of  $50.17 \pm 0.05$  pc (Gaia Collaboration 2020) in the constellation Puppis. HD 63754 is slightly metal-rich with a metallicity of  $[\text{Fe}/\text{H}] = 0.20 \pm 0.03$  dex (Brewer et al. 2016), a surface gravity of  $\log(g) = 4.04 \pm 0.06$  dex (Soubiran et al. 2016), an effective temperature of  $6088 \pm 32$  K (Soubiran et al. 2022), and a luminosity of  $4.88 \pm 0.01 L_{\odot}$  based on its Gaia G magnitude (Gaia Collaboration 2022). With above solar luminosity and effective temperature, HD 63754 A appears slightly evolved as a G-type main-sequence star. A summary of the stellar properties of HD 63754 A can be found in Table 1.

Using chromospheric activity as a proxy activity-age indicator, it is possible to attain an age estimate for HD 63754 A. The chromospheric activity index  $\log(R'_{\text{HK}})$ , measured by the S-index (Vaughan & Preston 1980; Duncan et al. 1991), is calculated by determining the ratio of the flux in a narrow bandpass centered on the Ca II H and K lines to the flux in two adjacent continuum bandpasses. HD 63754 has an S-index ranging from  $0.127$ – $0.139$  in the Pace (2013) catalog. Literature measurements report  $\log(R'_{\text{HK}})$  values of  $-5.12 \pm 0.07$  dex (Wright et al. 2004; Murgas et al. 2013; Brewer et al. 2016; Gomes da Silva et al. 2021), which favor an intermediate age for the system,

**Table 1.** Stellar Characteristics of HD 63754 A.

Property	Value	Refs
Host Star		
$\varpi$ (mas)	$19.93 \pm 0.02$	1
Distance (pc)	$50.17 \pm 0.03$	1
SpT	G0V	2
Mass ( $M_\odot$ )	$1.41 \pm 0.15$	13
Age (Gyr)	$> 3.4$	13
Radius ( $R_\odot$ )	$1.891 \pm 0.035$	8
$T_{\text{eff}}$ (K)	$6153 \pm 100$	3,4
[Fe/H] (dex)	$0.20 \pm 0.03$	3,4
log(g) (dex)	$4.04 \pm 0.06$	3,4
log( $R'_{\text{HK}}$ ) (dex)	$-5.12 \pm 0.07$	5,6,7,8
$R'_X$ (dex)	$< -4.28$	9
Gaia RUWE	1.023	1
Gaia G (mag)	$6.413 \pm 0.003$	1
$B_T$ (mag)	$7.235 \pm 0.066$	10
$V_T$ (mag)	$6.597 \pm 0.010$	10
$J$ (mag)	$5.486 \pm 0.034$	11
$H$ (mag)	$5.248 \pm 0.047$	11
$K_s$ (mag)	$5.133 \pm 0.023$	11
WISE W1 (mag)	$5.080 \pm 0.201$	12

NOTE: References abbreviated as (1) [Gaia Collaboration \(2020\)](#); (2) [Soubiran et al. \(2018\)](#); (3) [Soubiran et al. \(2018\)](#) (4) [Aguilera-Gómez et al. \(2018\)](#); (5) [Wright et al. \(2004\)](#); (6) [Murgas et al. \(2013\)](#); (7) [Brewer et al. \(2016\)](#); (8) [Gomes da Silva et al. \(2021\)](#); (9) [Voges et al. \(1999\)](#); (10) [Høg et al. \(2000\)](#); (11) [Cutri et al. \(2003\)](#); (12) [Cutri et al. \(2021\)](#); (13) This work

spanning the range of 2.4-3.57 Gyr ([Marsakov & Shevlev 1995](#); [Valenti & Fischer 2005](#); [Takeda et al. 2007](#); [Holmberg et al. 2009](#); [Delgado Mena et al. 2015](#); [Luck 2017](#); [Yee et al. 2017](#); [Delgado Mena et al. 2019](#)). We undertake an independent measurement of the stellar activity age using the Bayesian age-dating method outlined in [Brandt et al. \(2014\)](#) and applied in [Li et al. \(2021\)](#). This approach incorporates the X-ray ( $R_X$ ) and chromospheric activity ( $R'_{\text{HK}}$ ) indicators, along with the optional inclusion of rotation period to estimate ages using the calibrated activity-age relation provided by [Mamajek & Hillenbrand \(2008\)](#). We derive an activity-based age of  $\geq 3.4$  Gyr at a 68% confidence level given a chromospheric index value of  $\log(R'_{\text{HK}}) = -5.12 \pm 0.07$  and an X-ray index of  $R_X < -5.32$  from [Voges et al. \(1999\)](#). Figure 1 shows the activity-based posterior probability distribution for the age of HD 63754 A. Our result only offers a lower estimate of the stellar age and does not impose an upper limit. For comparison, BAFFLES ([Stanford-Moore et al. 2020](#)) yields age lower limits of  $> 6$  Gyr and  $> 3$  Gyr at 68% and 95% confidence levels, respectively, based on a chromospheric index of  $\log(R'_{\text{HK}}) \approx -5$  dex and a B-V color of  $B - V = 0.58 \pm 0.002$  ([ESA 1997](#)). Note that these lower limits from BAFFLES are marginally underestimated because we used an approximated chromospheric index due to the calibration range limited to -5 dex in [Stanford-Moore et al. \(2020\)](#). In all scenarios, our result is consistent with the prevailing literature measurements supporting an intermediate age for the star, most likely slightly younger than the Sun ([Costa Silva et al. 2020](#); [Delgado Mena et al. 2019](#); [Llorente de Andrés et al. 2021](#); [Palla et al. 2022](#); [Luck 2017](#)).

The mass of HD 63754 A has also been the subject of various studies. [Bochanski et al. \(2018\)](#) matched the Gaia observations with data from the 2MASS and Wide-Field Infrared Survey Explorer catalogs, and applied MIST isochrones to derive an estimate of  $1.46 \pm 0.05 M_\odot$  for HD 63754 A among a sample of co-moving stars. [Anders et al. \(2019\)](#) obtained a mass of  $1.27 \pm 0.19 M_\odot$  by melding photometric and astrometric data from Gaia EDR3 with stellar evolutionary models. [Gomes da Silva et al. \(2021\)](#) analyzed HARPS spectra and

determined a mass of  $1.426 \pm 0.017 M_\odot$ , while [Pägert et al. \(2021\)](#) utilized Bayesian inference with Gaia parallax data, obtaining a mass of  $1.12 \pm 0.15 M_\odot$  for the TESS input catalog. While the literature currently contains a range of mass estimates, astroseismology with TESS could enable a more accurate determination of the host star's mass. We independently determined the stellar mass with the PARSEC isochrone stellar evolution models ([Bressan et al. 2012](#)) following [Li et al. \(2021\)](#). We derive a mass of  $1.41 \pm 0.05 M_\odot$  that is consistent with the literature. Due to the diverse mass estimates found in the literature, we not only consider our mass estimate of  $1.41 \pm 0.05 M_\odot$  as a stellar mass prior in Section 5, but also explore a broader stellar mass prior of  $1.41 \pm 0.15 M_\odot$  to encompass the range of values reported in previous studies.

### 3 THE PREDICTED COMPANION FROM RV AND ABSOLUTE ASTROMETRY

In 2021, we initiated a pilot direct imaging survey program at the Keck Observatory to find companions around accelerating stars. [Brandt et al. \(2019\)](#) has shown that stars demonstrating significant ( $\geq 3\sigma$ ) disparities between *Hipparcos* and *Gaia* proper motions in the cross-calibrated *Hipparcos-Gaia* Catalog of Accelerations (HGCA) ([Brandt 2018, 2021](#)) point to potential hosts of unseen companions. Our target selection strategy uses HGCA as a tool to identify stars with notable proper motion anomalies between *Hipparcos* and *Gaia*. In addition, stars with known radial velocities allow us to utilize both HGCA data and the RVs to jointly fit their orbits using the MCMC orbit code *orvara* [Brandt et al. \(2021c\)](#) before initiating observations. This precursor information garnered from the RV and HGCA astrometry orbital fit enables us to predict potential locations of companions for follow-up imaging efforts. The combination of an HGCA-based target vetting strategy and *orvara* location predictions represents a novel approach to improve high-contrast imaging yields, as demonstrated by the success of several other highly productive imaging surveys such as [Fontanive et al. \(2019\)](#); [Currie et al. \(2021\)](#); [Bowler et al. \(2021\)](#); [Bonavita et al. \(2022\)](#); [Franson et al. \(2022\)](#); [Rickman et al. \(2022\)](#).

HD 63754 B was selected for our pilot program with a vetting technique similar to that discussed in [Franson & Bowler \(2023\)](#), which involves calculating joint probability maps in separation and companion mass for stars with significant low-amplitude HGCA accelerations. The probability maps predict allowed and disallowed zones for potential companions around accelerating host stars based on their accelerations in the HGCA, helping evaluate the potential discovery space. We also conduct preliminary MCMC orbital retrieval using *orvara* and RV+HGCA data to predict the location of potential companions at specified observation epochs for subsequent direct imaging observations.

#### 3.1 Absolute Astrometry

The absolute astrometry of HD 63754 A is taken from the Gaia EDR3 version of the *Hipparcos-Gaia* Catalog of Accelerations (HGCA, [Brandt \(2021\)](#)). The HGCA is a cross-calibration of the *Hipparcos* and *Gaia* EDR3 catalogues onto a common reference frame with well-characterized uncertainties. The HGCA compares the 25-year *Hipparcos-Gaia* scaled positional difference, the *Hipparcos* proper motion (near 1991.25), and the *Gaia* EDR3 proper motion (near 2016.0). Different proper motions suggest reflex motion of the star due to the tug of a massive companion.

**Table 2.** HGCA absolute astrometry for HD 63754 A.

Parameter	Hipparcos	Hipparcos-Gaia	Gaia EDR3
$\mu_{\alpha^*}$ (mas yr $^{-1}$ )	$-35.748 \pm 0.492$	$-33.565 \pm 0.016$	$-33.726 \pm 0.025$
$\mu_{\delta}$ (mas yr $^{-1}$ )	$-129.582 \pm 0.386$	$-127.543 \pm 0.013$	$-125.768 \pm 0.025$
corr( $\mu_{\alpha^*}, \mu_{\delta}$ )	0.237	0.177	-0.086
$t_{\alpha}$ (Jyr)	1991.33	-	2015.87
$t_{\delta}$ (Jyr)	1991.48	-	2015.85

NOTE: The  $\chi^2$  value for a model of constant proper motion (Hipparcos-Gaia and Gaia proper motions are equal) is 4056 with two degrees of freedom.

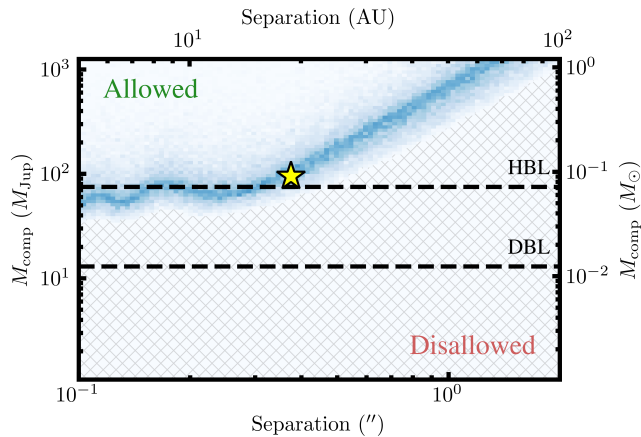


**Figure 2.** Predicted mass of HD 63754 B as a function of projected separation based on the *Hipparcos-Gaia* proper motion anomaly of its host star HD 63754 A. The color gradient indicates the relative probability of agreement between the predicted astrometric mass and the dynamical mass, with companions below the blue curve unable to account for the observed change in proper motion. HD 63754's astrometric acceleration points to a substellar companion within 0.2" or a more distant star. Dotted lines mark the Hydrogen Burning Limit (HBL) of  $\sim 75 M_{\text{Jup}}$  and the Deuterium-burning limit (DBL) of  $\sim 13 M_{\text{Jup}}$ . The yellow star represents HD 63754 B's predicted dynamical mass ( $95^{+25}_{-19} M_{\text{Jup}}$ ), eccentricity ( $\sim 0.26$ ) and separation ( $\sim 0.4"$ ) based on the RV+HGCA `orvara` fit in Section 3.3, predating direct imaging observations.

HD 63754 A was selected for our program as it experiences proper-motion differences of  $\approx 64\sigma$  in the HGCA, suggesting the existence of a massive companion. Table 2 lists HD 63754 A's absolute astrometry from the HGCA, including the Hipparcos proper motion, the Gaia DR3 proper motion, and a joint Hipparcos-Gaia positional difference divided by the temporal baseline between the two missions. The Renormalized Unit Weight Error (RUWE) metric is used to assess the quality of astrometric solutions provided by Gaia, with values close to 1 indicating a good fit between the observations and the expected behavior of a single star. The RUWE for HD 63754 in Gaia is 1.02 (Gaia Collaboration 2020), well below the threshold of 1.4 at which the Gaia pipeline attempts a non-single star solution. This indicates that the Gaia observations for HD 63754 are consistent with a satisfactory single-star solution: there is little orbital curvature within the Gaia data.

### 3.2 Radial Velocity

The RV of the system was monitored by both HARPS and HIRES. The HARPS and HIRES radial velocity data do not cover the full orbital period, but suggest a shallow trend for HD 63754 A, indi-

cating the presence of a distant companion. The HIRES RVs are acquired from the High Resolution Echelle Spectrograph (HIRES) (Vogt & Keane 1993) positioned at the right Nasmyth focus of the Keck-1 telescope. These RVs encompass observations both before and after the 2004 CCD upgrade, collectively demonstrating an rms value of 26.3 m/s, with a median uncertainty of 1.9 m/s for each individual measurement. The High Accuracy Radial Velocity Planet Searcher (HARPS) spectrograph was installed in 2002 on the ESO's 3.6m telescope at La Silla Observatory in Chile. The HARPS RVs exhibit an rms value of 13.0 m/s and a median uncertainty on each individual measurement of 1.46 m/s. We fetch the data from the HARPS-RVBANK's (Trifonov et al. 2020) "DRVmlcnzp" column, which corrects for zero-point variations, intra-night RV drift, and an absolute RV offset attributed to the upgrade of the HARPS fibers in 2015. In our orbit analysis, we treat the RV datasets from both the HARPS and HIRES before and after the fiber upgrades as separate instruments with distinct RV zero points. In total, we consider four instruments and four RV datasets.

### 3.3 Predicted Location

First, we use RVs and absolute astrometry as described above to perform an orbital fit to the HD 63754 system. In addition to modeling the orbital parameters, `orvara` allows for the generation of 1-, 2-, and 3- $\sigma$  likelihood contours that illustrate the potential coordinates of the companion relative to its host star at any given epoch. The initial results from the RV and absolute astrometry fit indicate the presence of a massive stellar companion of  $95^{+25}_{-19} M_{\text{Jup}}$  orbiting HD 63754 A at a distance of  $18.8^{+10}_{-4.8}$  AU. We show the predicted 3- $\sigma$  contours outlining the potential positions of the companion in the left panel of Figure 3. The RVs and absolute astrometry point to a companion west of the star, with mean predicted separations in RA and Dec at 2023.0 of  $-390 \pm 160$  mas and  $180 \pm 150$  mas, respectively.

We also compute joint probability maps in separation and companion mass for HD 63754 A based on its HGCA astrometric accelerations following (Franson et al. 2023). This involves the generation of 100 circular orbits with random orientations for each grid point in semi-major axis-companion mass space. The resultant acceleration distribution is then juxtaposed with the star's average acceleration and uncertainty, employing the K-S statistic (Kopytova et al. 2016). The mass prediction based on HD 63754 A's acceleration is showcased in Figure 2, suggesting the existence of either a brown dwarf within 0.2" or a stellar companion beyond 0.2". Our predicted companion, represented by the yellow star in the RV+HGCA only fit, indicates a stellar companion with a dynamical mass of  $95^{+25}_{-19} M_{\text{Jup}}$  at a separation of  $\sim 0.4"$ . The preliminary RV+HGCA fit places the stellar companion within the allowed zone, hinting at the possibility of discovery. However, the orbit of the companion is subject to variability as direct imaging observations are incorporated. In the next section, we describe our thermal infrared imaging discovery of the predicted companion HD 63754 B.

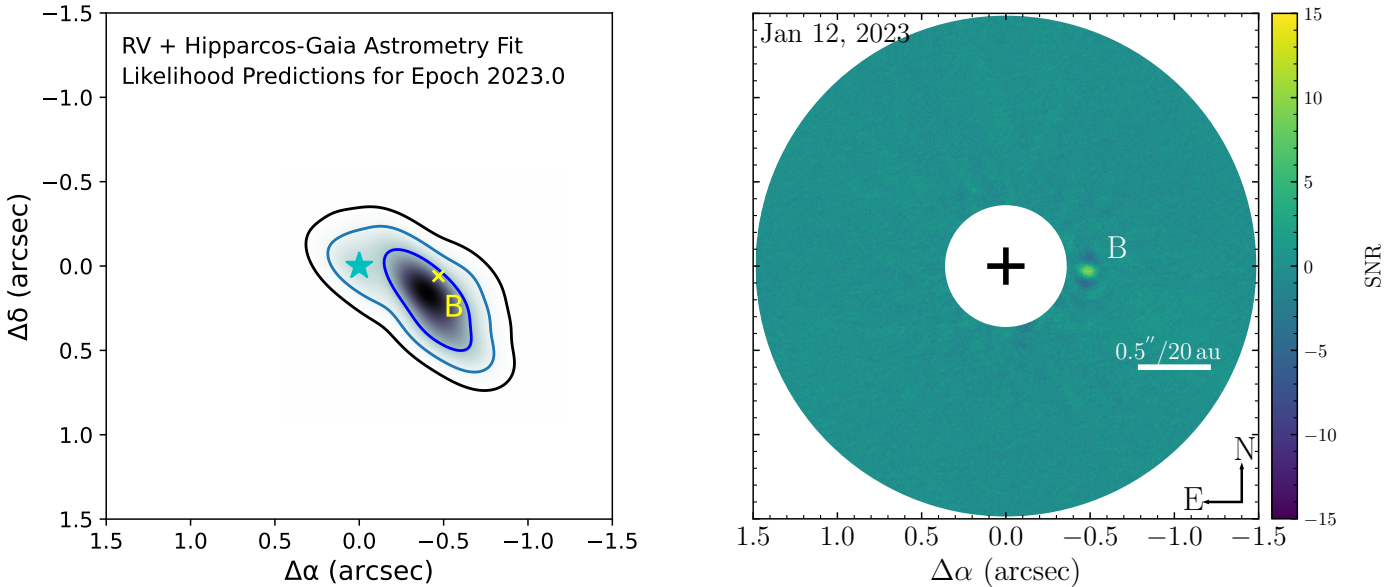


**Figure 3.** (Left) The blue probability contours depict the predicted position (1, 2, and 3 $\sigma$ ) of HD 63754 B relative to its host star (cyan). The companion's location was constrained by fitting archival radial velocities from HARPS and HIRES, and Hipparcos-Gaia absolute astrometry with the `orvara` orbit fitting package [Brandt et al. \(2021c\)](#). The yellow cross shows where it was imaged. (Right) PCA PSF subtracted image with nine principle components showing the detection of the companion within the edge of its predicted 1- $\sigma$  likelihood contour. The SNR of the detection is 12.5.

#### 4 KECK/NIRC2 OBSERVATION AND DATA REDUCTION

We observed the HD 63754 system with the thermal Near-Infrared Camera 2 (NIRC2) at the Keck Observatory in the  $L'$ -band (central wavelength  $3.8\ \mu m$ ) on UT 2023 Jan 11. We use the narrow camera with a pixel plate scale of  $9.971 \pm 0.004$  mas/pixel ([Service et al. 2016](#)) and a  $512 \times 512$  pixel subarray. The NIRC2 data were taken behind the Vector Vortex Coronagraph (VVC; [Serabyn et al. 2017](#)) with a vortex phase mask using natural guide star AO and the visible-light Shack-Hartmann wave-front sensor. The seeing conditions for the night were roughly photometric, with an average value of  $1.^{\prime\prime}0 \pm 0.^{\prime\prime}3$  as seen by the differential image motion monitor (DIMM). The observations involve sequences of 20-30 science frames using the Quadrant Analysis of Coronagraphic Images for Tip-Tilt Sensing (QACITS) algorithm. This algorithm applies small tip-tilt corrections to re-center the star after each exposure, achieving milliarcsecond stability ([Huby et al. 2015, 2017](#)). We also incorporate a 4.5 mas QACITS centering uncertainty from [Huby et al. \(2017\)](#) to account for the average pointing accuracy from the QACITS controller. This centering uncertainty is divided by the separation measurement and added in quadrature to the position angle uncertainty. Each sequence also includes an off-axis unsaturated frame for flux calibration and sky-background frames for both the science images and the point-spread-function (PSF) images. We captured a total of 165 science images, excluding 9 short pointing optimization frames. Each frame consisted of 90 coadds with 0.3s exposures to for optimal readout efficiency. The total integration time was 4590s (76.5 minutes), accompanied by a field rotation of  $35^{\circ}$ .

We process our imaging sequence using Angular Differential Imaging (ADI) with the Vortex Image Processing (VIP) package ([Gomez Gonzalez et al. 2017](#)). VIP is specifically designed for processing vortex coronagraphic observations. We first flat field and dark subtract our science images. Then we employ the `lacosmic` Python

package to remove cosmic rays ([van Dokkum 2001](#)), and we correct for geometric distortion using the solutions provided by [Service et al. \(2016\)](#) for the narrow-field mode of the NIRC2 camera. To enhance the signal-to-noise ratio (SNR), we employ VIP to model and subtract the sky background in both the science frames and the off-axis flux-calibration frames. Precise centering of the images is crucial in ADI reduction to ensure proper alignment of the vortex with the center of the field of view. We fit a 2D Gaussian to the vortex's core halo in each image while determining the centroid. For each time slice, we cut a subimage centered around the centroid we have determined so that the images are aligned properly at the mas level between frames. The alignment uncertainty is gauged by computing the standard deviation of the centroid from the image center. The total alignment error, including QACITS centroiding uncertainty, averages around 5.0 mas.

VIP offers PCA-based postprocessing algorithms ([Soummer et al. 2012; Amara & Quanz 2012](#)) for stellar point spread function (PSF) subtraction. The PSF is obtained by subtracting the sky-background frame from the PSF image with the star off the vortex. By fitting a 2D Gaussian profile to the host-star's sky-subtracted PSF, we measure a mean FWHM value of 7.89 pixels ( $0.079''$ ). Here we use the same procedure outlined in [Li et al. \(2023\)](#) to do PSF subtraction. Unlike simple median combination of ADI, PCA algorithms enhance the contrast by modeling the background including leaked starlight, static and quasi-static speckles. This is achieved by projecting each image onto the first  $n$  principal components, obtained through singular value decomposition of a 2D matrix created from the observed sequence of images. This approach removes the stellar PSF from each image in HD 63754 A's data cube by subtracting principal components from individual annular regions. This highlights fainter and more extended structures like planets or disks. To reduce self-subtraction, we employ a rotation gap/PA threshold and radial scaling criterion ([Lafrenière](#)

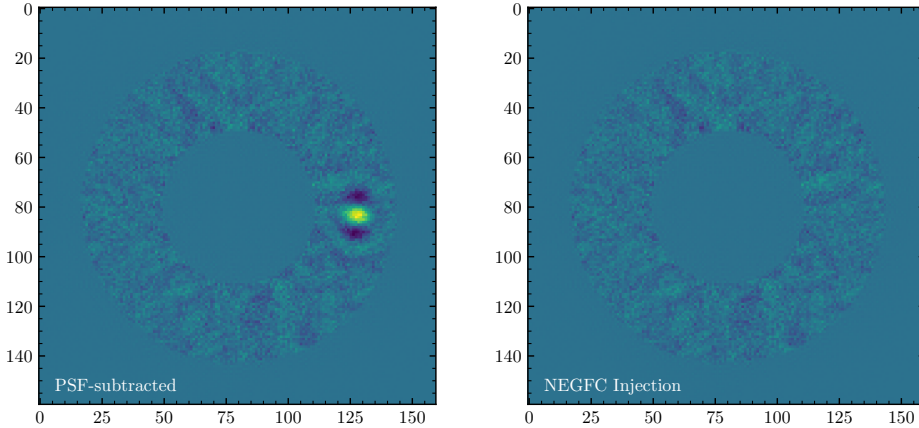


**Figure 4.** PSF-subtracted image of HD 63754 B (left) and the same image after introducing negative PSF templates with optimal separations, position angles, and flux ratios (right). The negative companion injection successfully eliminates companion signals in the latter image.

et al. 2007) in annular patches, discarding frames with inadequate rotation. Specifically, using VIP, we find that setting a PA threshold of 0.3 FWHM, or  $\delta > 0.31/D$ , where  $\lambda$  is the observing wavelength and  $D$  is the diameter of the telescope’s primary mirror, best ensures that the companion is not inadvertently subtracted during the image processing. We also tune the optimal number of components that would optimize the SNR by running PSF subtractions from 1 to 30 components, measuring the resultant companion SNR each time in the reduced images. SNR is determined using the method outlined in Mawet et al. (2014), which incorporates a penalty at small separations to account for the limited number of resolution elements. We found that the highest SNR is produced by using 9 components. We detected the companion with a signal-to-noise ratio (SNR) of 12.5 using annular PCA. Figure 3 shows the detection of a point source with PCA subtraction, which we refer to as HD 63754 B, roughly 47.2 pixels or  $0''.471$  from the star. HD 63754 B is the only object identified by NIRC2 within  $1''$ . We visually inspect the Standardized Trajectory Intensity Map (STIM; Pairet et al. (2019)), which did not show any presence of other signals.

The negative fake companion (NEGFC) technique (Marois et al. 2010; Lagrange et al. 2010; Wertz et al. 2017) is often used in conjunction with principal component analysis (PCA) or other PSF subtraction methods to accurately extract the position and flux of point-like sources, particularly for faint companions close to bright stars. The use of NEGFC avoids biases in astrometry and photometry from partial and self-subtraction. The NEGFC technique works by injecting a negative-amplitude PSF template at the location of the companion, effectively removing the signal from the true companion in the final image. This allows for a more accurate measurement of the true companion flux and position. NEGFC has been shown to be more effective for faint companions closer to the primary star, which can be easily affected by residual speckles or other systematic artifacts. We show the PSF-subtracted signal alongside the result after NEGFC injection in Figure 4.

Using VIP, we take the astrometric and photometric measurements from annular PCA as initial conditions for the iterative NEGFC calculations. First, we utilize the Nelder-Mead downhill simplex optimization algorithm (Nelder & Mead 1965) to provide the initial guesses that would be used as a starting state in MCMC optimization. Next, we explore the 3D parameter space of the flux within the aperture and polar positions using the emcee affine-invariant Markov Chain Monte Carlo (MCMC) ensemble sampler introduced by Foreman-

**Table 3.** Keck/NIRC2 relative astrometry and  $L'$ -band photometric measurements of the HD 63754 AB system

HD 63754 AB	
Instrument	Keck/NIRC2
Filter	$L'$
Date (UT)	2023-01-11
Epoch (yr)	2023.03
Relative Astrometry	
Separation (mas)	$473.3 \pm 5.2$
PA (°)	$277.89 \pm 0.14$
Photometry	
$\Delta L'$ (mag)	$9.78 \pm 0.06$
$L'_*$ Flux (mag)	$5.11 \pm 0.05$
$L'_P$ Flux (mag)	$14.89 \pm 0.06$

NOTE: The  $L'$  magnitude for the host star is transformed from its 2MASS H band magnitude using relations in Bessell & Brett (1988).

Mackey et al. (2013). We run 100 walkers, each taking 1000 steps, resulting in a total of  $10^5$  steps. We use the auto-correlation time based criterion  $N/\tau \geq a_c$  with  $a_c = 50$  (Christiaens et al. 2021) to evaluate convergence. To ensure reliable results, we discard the first 30% of each chain as burn-in. We run the fit multiple times to ensure consistent and identical astrometry and photometry results for each run. We further correct for throughput and the ratio of exposure times between stellar PSF frames (100 coadds with 0.008 integration time per coadd) and the science frames that contain the companion (90 coadds and 0.3s exposures). The errors on the astrometry are calculated by adding in quadrature the uncertainties from the MCMC NEGFC injection technique, our pre-processing alignment uncertainty of 0.5 mas which includes the QACITS centroiding uncertainty of 0.2 pixels. We correct for the position angle from the NEGFC reduction  $\theta_{\text{meas}}$  through

$$\theta = \theta_{\text{meas}} - (\text{PARANG} + \text{ROTPASN} - \text{INSTANGL} - \theta_{\text{north}}) \quad (1)$$

where PARANG is the parallactic angle offset, ROTPOSN is the rotator position of  $4^\circ 43$ , INSTANGL is the NIRC2 position angle zero-point of  $0^\circ 7$ , and  $\theta_{\text{north}} = 0^\circ 262 \pm 0^\circ 020$  (Service et al. 2016) is the angle we applied to rotate the frames counterclockwise in order for them to have a North-up and East-left orientation. We measure a corrected position angle of  $277^\circ 89 \pm 0^\circ 14$  south-west from the primary star. Our final astrometry results based on the NEGFC approach are listed in listed in Table 3.

Given the lack of a multi-wavelength spectrum for HD 63754 B, our capacity to determine its spectral type is limited to deducing a bolometric luminosity from its  $L'$  band brightness, followed by comparison to field brown dwarfs with known spectra. We infer a bolometric luminosity for HD 63754 B based on its  $L'$  band magnitude using a method outlined in Li et al. (2023). First, we measure an  $L'$  contrast between the star and the companion of  $9.79 \pm 0.06$  mag. The  $L'$  magnitude of the star is  $5.11 \pm 0.05$  magnitudes, obtained through transformation from the 2MASS H band magnitude using a relation detailed in Bessell & Brett (1988). This establishes the  $L'$  mag for HD 63754 B as  $L'_p = 14.89 \pm 0.06$  mag, which corresponds to an absolute magnitude of  $L'_p = 11.39 \pm 0.06$  mag based on the parallax. We transform this absolute  $L'$  band magnitude into an absolute magnitude in the  $W1$  band of  $M_{W1} = 12.20 \pm 0.07$  mag according to the relation derived by Franson et al. (2023). To retrieve the bolometric luminosity, we convert the absolute magnitude in the  $W1$  band by fitting a fourth order polynomial to a segment of Filipazzo et al. (2015) spectral energy distribution (SED) for a comprehensive sample of field dwarfs complied from legacy surveys. The uncertainty on the bolometric luminosity include the error in the  $L'$  band contrast, the scatter in the  $L'$  to  $W1$  conversion by Franson et al. (2023), and the uncertainty in our fourth order polynomial fit converting  $W1$  to bolometric luminosity. Overall error propagation resulted in a final bolometric luminosity of  $\log(L_{\text{bol}}/L_{\odot}) = -4.55 \pm 0.08$  dex for HD 63754 B. This luminosity implies that the companion resides in close proximity to the L/T transition.

## 5 ORBITAL CONSTRAINTS

We model the 3D orbit of HD 63754 B with the Bayesian orbit fitting code `orvara` (Brandt et al. 2021c), incorporating HGCA absolute astrometry, HIRES and HARPS RVs, and single-epoch relative astrometry from our Keck/NIRC2  $L'$  band imaging. The `orvara` code employs parallel tempering MCMC (PT-MCMC) with the `emcee` ensemble sampler (Foreman-Mackey et al. 2013; Vousden et al. 2015) to sample posterior orbital parameters. PT-MCMC involves running parallel chains at varying temperatures for precise sampling around the minimum  $\chi^2$  within the parameter space; chains periodically exchange positions to enhance sampling efficiency. Our PT-MCMC process utilized 100 walkers, 30 temperatures, and a total of  $10^5$  steps. `orvara` fits six orbital elements that fully describe a Keplerian orbit, plus two masses and an RV jitter term. The optimization speeds up parameter fitting by analytically handling auxiliary parameters like RV zero-points and parallax.

We first impose an informative prior of  $1.41 \pm 0.05 M_{\odot}$  on the mass of HD 63754 A, covering the range of literature measurements as discussed in Section 2. We apply uninformative priors on all other fitted parameters: flat priors on the eccentricity, argument of periastron, mean longitude, and ascending node, and log-flat priors on the mass of the companion, semi-major axis and RV jitter, and geometric priors on the inclination. We assess convergence via visual inspection and discard the initial 40% of the chain as burn-in. We verify that variations in the burn-in threshold beyond 40% have marginal effects on resultant posteriors and consistently yield the same inferred parameters. Using this putative informative prior on the host star's mass, we obtain a dynamical mass of  $80.0^{+4.4}_{-3.2} M_{\text{Jup}}$ , a semi-major axis of  $19.9^{+2.8}_{-1.7}$  AU, an eccentricity of  $0.262^{+0.060}_{-0.046}$ , and an inclination of  $174.82^{+0.47}_{-0.50}$ . To account for the uncertainty linked to the host star's mass, we also explore a broader prior of  $1.41 \pm 0.15 M_{\odot}$ . With this wider prior we measure a dynamical mass of  $81.9^{+6.4}_{-5.8} M_{\text{Jup}}$  for

the companion, a semi-major axis of  $19.9^{+2.7}_{-1.6}$  AU, an eccentricity of  $0.260^{+0.065}_{-0.059}$ , and an almost face-on inclination of  $174.81^{+0.48}_{-0.50}$ . The corner plot illustrating the correlations among selected parameters for the informative prior of  $1.41 \pm 0.05 M_{\odot}$  and the narrowed prior are shown in Figure 10 and Figure 11, respectively.

Table 4 enumerates the orbital parameters inferred from our MCMC posteriors. In Figure 5, we provide an illustrative selection of 50 orbits, randomly sampled from the posterior distributions, which showcase the relative orbit projected onto the sky plane, the RV fit, and the astrometric fit to the HGCA proper motions. The best fit orbit is represented by the black curve among the colorful randomly sampled orbits. The Hipparcos and Gaia proper motions are both formal good fits to the astrometric reflex motion of the star (a total  $\chi^2 = 1.6$ ), with Gaia providing the more precise measurement of the two. The HARPS and HIRES combined RV measurements and our solitary astrometric data point cover only a segment of the orbit around aphelion, contributing to slightly better convergence in that orbital region. The lack of phase coverage by both RV and relative astrometry collectively contributes to the uncertainty in the orbital fit. We find a range of potential orbital solutions with fluctuations within a 6% uncertainty in the companion mass.

## 6 DISCUSSION

### 6.1 Measured Properties of HD 63754 B

The Hydrogen-Burning Limit (HBL) is the minimum mass required for thermonuclear fusion in a star's core; it distinguishes brown dwarfs from low-mass stars. The accurate delineation of the HBL relies on factors like the equation of state, rotation, composition, and atmospheric attributes (Burrows et al. 1997), generally falling within the range of  $70\text{--}80 M_{\text{Jup}}$ . If adopting  $75 M_{\text{Jup}}$  as the HBL, 14% of our dynamical mass posterior distribution falls below the HBL, and 86% lies above this value. If we instead adopt Chabrier et al. (2023)'s new estimate for the HBL of  $78.5 M_{\text{Jup}}$  that accounts for previously neglected physical effects, then 31% of our MCMC mass posterior lies below the substellar boundary. Alternatively, using the dynamical mass posterior from a narrow prior of  $1.41 \pm 0.05 M_{\odot}$  for the primary star, 11% and 38% of the mass posterior are below a HBL of  $75$  and  $78.5 M_{\text{Jup}}$ , respectively. Our dynamical mass of  $81.9^{+6.4}_{-5.8} M_{\text{Jup}}$  at 68% confidence cannot definitively classify it as either a brown dwarf or a low-mass star. However, the luminosity of HD 63754 B, inferred from its  $L'$  photometry, suggests that the color of HD 63754 B more closely aligns with a substellar nature – specifically, indicating a massive brown dwarf near the L/T transition.

The orbital eccentricities of substellar companions also shed light on key processes during their formation. Recent population-level inferences of 27 long-period giant planets and brown dwarfs (5–100 AU) by Bowler et al. (2020) and Nagpal et al. (2023) reveal distinct eccentricity distributions for giant planets ( $e \approx 0.05\text{--}0.25$ ) and brown dwarfs ( $e \approx 0.6\text{--}0.9$ ). This dichotomy suggests different formation channels: planets may form within protoplanetary disks, while brown dwarf genesis may occur through cloud fragmentation, resembling the formation channel of wide stellar binaries. HD 63754 B, orbiting at  $\sim 20$  AU with a tightly constrained eccentricity of  $0.260^{+0.065}_{-0.059}$ , exhibits a lower eccentricity than the broad peak toward high values ( $e \approx 0.6\text{--}0.9$ ) found for 18 imaged brown dwarf companions in Bowler et al. (2020). Further, they found that brown dwarf companions on closer orbits (5–30 AU) have a lower eccentricity distribution peak at  $e \approx 0.5$  compared to those at wider separations (30–100 AU), which peak at  $e \approx 0.74$ . By both standards, HD 63754 B has a notably

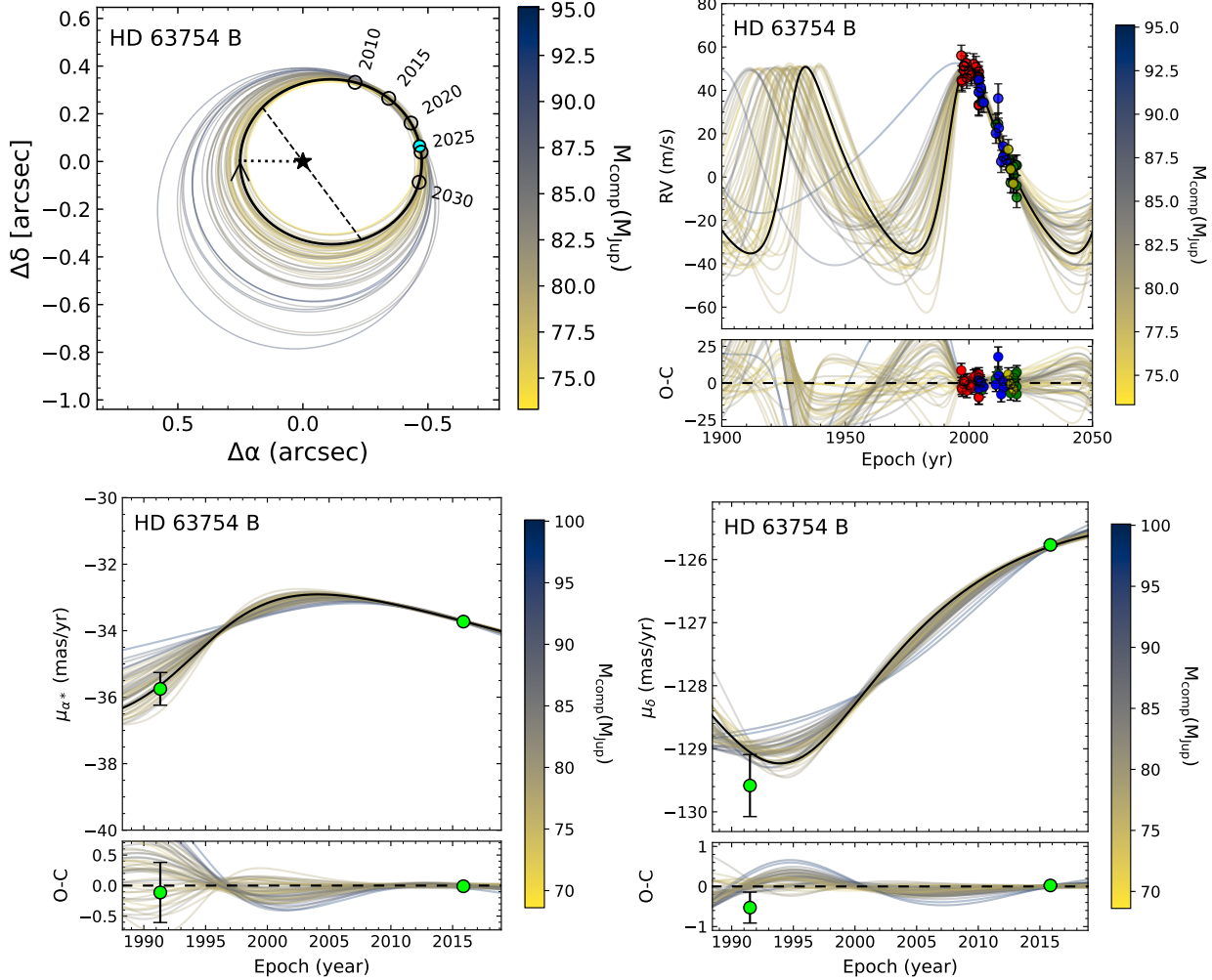


**Figure 5.** Orbit fit of the HD 63754 AB system, including the sky-projected orbit (top left), RVs (top right), and HGCA proper motions (bottom panels). The colorful curves represent 50 randomly drawn orbits from the MCMC chains, while the maximum-likelihood orbit is highlighted in black. The red, blue, yellow, and green data points in the RV datasets are from the HARPS pre-fiber update, HARPS post-fiber update, HIRES pre-fiber update, and HIRES post-fiber update, respectively. The green points in the lower panels represent the Hipparcos and Gaia EDR3 proper motions; the measured long-term proper motion (not shown) constrains the integral of the proper motion.

lower eccentricity. One possibility could be the presence of additional companions that circularized its orbit, as observed in stable, multi-planet systems like HR 8799 (Bowler et al. 2020). In any scenarios, HD 63754 B provides a valuable data point for such eccentricity studies of directly imaged brown dwarfs.

Our orbital inclination also suggests that HD 63754 B's orbital orientation is close to being face-on as observed from the Earth. The near-face-on orbit would explain the significant astrometric acceleration of  $64\sigma$  in the HGCA, but subdued RV signal despite it being a massive candidate. We note that this is due to selection biases in the astrometric detection and recovery with imaging of companions found using accelerations. Continued direct imaging monitoring will enhance the precision of the companion's measured mass and orbit.

## 6.2 Comparison to Evolutionary Models

We compare the independent mass, age, and luminosity measurements of HD 63754 B with three models of substellar evolution that provide self-consistent calculations for atmospheric structure and evolution across varying assumptions of atmospheric chemistry and boundary conditions. We consider the cloudless model TUSCON by Burrows et al. (1997), the cloudless ATMO-2020 model by Phillips et al. (2020), and the Saumon et al. (2008) hybrid model with a mixture of cloud prescriptions (no clouds, hybrid, and cloudy). The Burrows et al. (1997) TUSCON model uses lower-opacity 'gray' atmospheres at higher temperatures, particularly intended for cloud-free cooler brown dwarfs below 1300 K. The Phillips et al. (2020) ATMO-2020 model is an updated cloud-free model compared to TUSCON, following the same lineage as the "Cond" (Baraffe et al. 2003) and "BHAC15" (Baraffe et al. 2015) models. Both the TUSCON and ATMO 2020 cloudless models are designed specifically

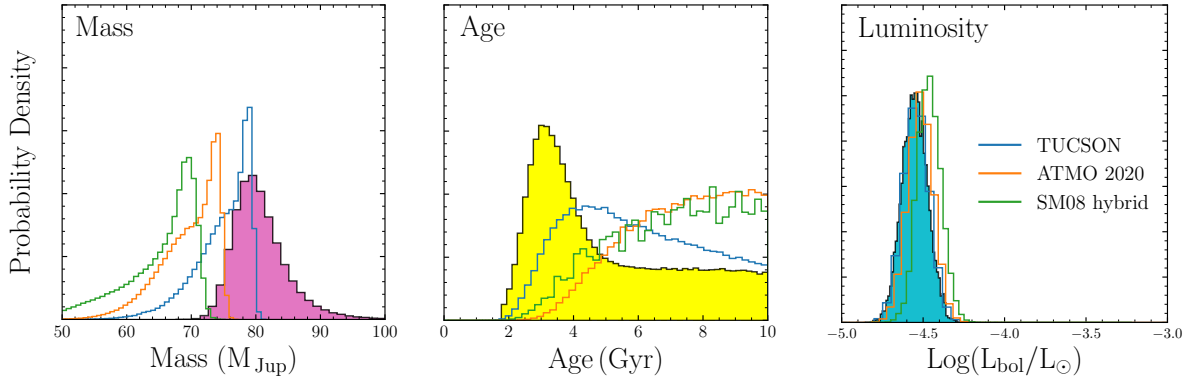


**Figure 6.** Comparison between predicted masses and ages from evolutionary models and the dynamical mass and age of HD 63754 B. (Left) Posterior distribution of dynamical mass (filled magenta histogram) compared to model-derived mass posteriors for the inferred distributions of  $L_{\text{bol}}$  and host star age. (Right) Posterior distribution of age sampled with evolutionary models from the inferred mass and luminosity. The filled yellow distribution represents the posterior from our Bayesian isochrone age-dating model. With a flat prior on age, all evolutionary models favor moderate to older ages for the system; this is due to the high measured mass and low luminosity.

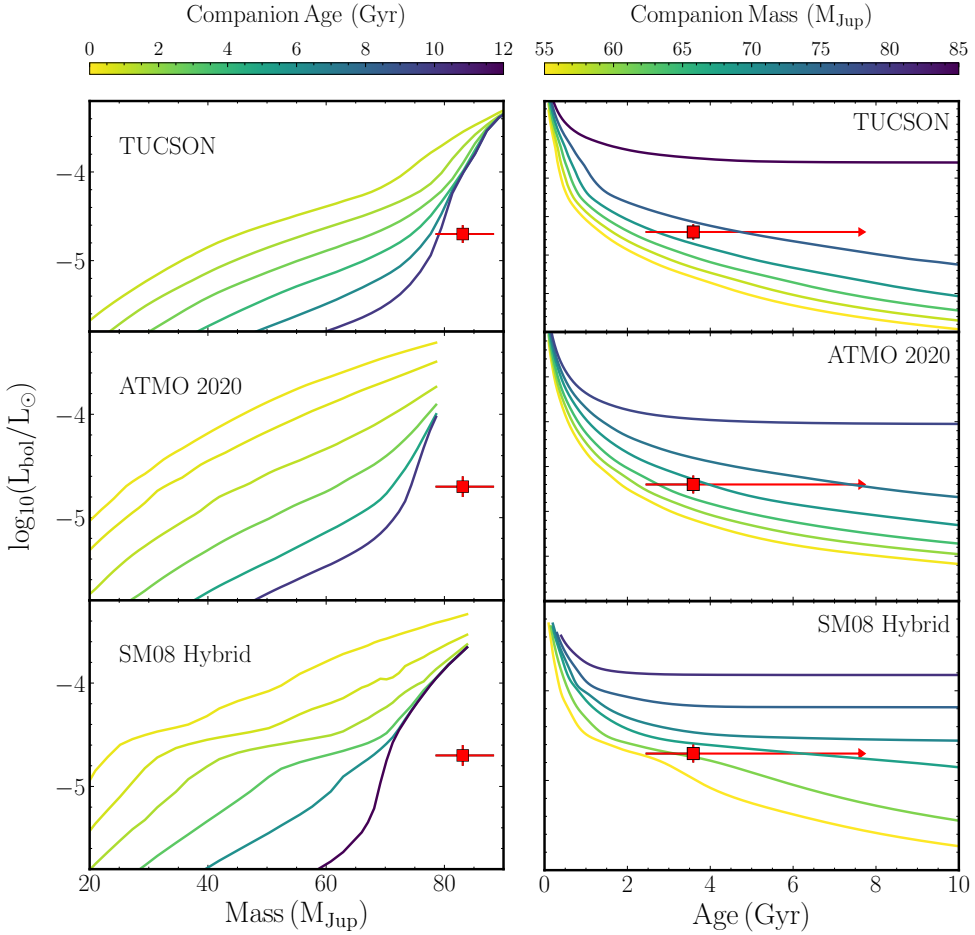


**Figure 7.** Comparison of the dynamical mass, luminosity and age of HD 63754 B with the predicted masses and ages from three evolutionary models. Left panels show the age-luminosity plot and the iso-mass evolutionary grids from the three models. Right panels present the iso-age evolutionary grids. The grids are color-coded by the companion age and mass, respectively. The observed properties for HD 63754 B are indicated by the red square markers with errorbars. The overestimation of the dynamical mass and/or underestimation of bolometric luminosity could explain why the red data points fall outside the model grids in the left panels.

**Table 4.** MCMC orbital fit results for HD 63754 B with the narrow Gaussian prior of  $1.35 \pm 0.15 M_{\odot}$  on the host star's mass.

Parameter	Prior	Best Fit	68.3% CI	95.4% CI
Fitted Parameters				
$\sigma_{\text{Jit}}$ (m/s)	$1/\sigma_{\text{Jit}}$	4.41	$4.41^{+0.64}_{-0.54}$	(3.413, 5.794)
$M_*$ ( $M_{\odot}$ )	$N(0.72, 0.02)$	1.40	$1.40^{+0.14}_{-0.14}$	(1.122, 1.685)
$M_p$ ( $M_{\odot}$ )	$1/M_p$	81.9	$81.9^{+6.4}_{-5.8}$	(70.663, 96.243)
$a$ (AU)	1/a	19.9	$19.9^{+2.7}_{-1.6}$	(17.251, 27.878)
$\sqrt{e} \sin \omega$	$U(-1, 1)$	-0.27	$-0.27^{+0.34}_{-0.20}$	(-0.581, 0.432)
$\sqrt{e} \cos \omega$	$U(-1, 1)$	0.384	$0.384^{+0.083}_{-0.12}$	(0.129, 0.529)
$i$ ( $^{\circ}$ )	$\sin i$	174.81	$174.81^{+0.48}_{-0.50}$	(173.781, 175.731)
$\Omega$ ( $^{\circ}$ )	$U(-180, 180)$	40.2	$40.2^{+8.1}_{-7.1}$	(26.613, 57.906)
$\lambda_{\text{ref}}$ ( $^{\circ}$ )	$U(-180, 180)$	40.4	$40.4^{+11}_{-8.4}$	(25.176, 64.963)
Derived Parameters				
$\varpi$ (mas)	–	19.9319	$19.9319^{+0.0016}_{-0.0016}$	(19.929, 19.935)
$P$ (yr)	–	73.4	$73.4^{+16}_{-9.4}$	(58.044, 123.531)
$\omega$ ( $^{\circ}$ )	–	311	$311^{+28}_{-271}$	(4.301, 356.042)
$e$	–	0.260	$0.260^{+0.065}_{-0.059}$	(0.148, 0.393)
$a$ (mas)	–	397	$397^{+54}_{-33}$	(344, 556)
$T_0$	–	2476422	$2476422^{+7530}_{-4083}$	(2470000, 2496000)

NOTE: The reference epoch is 2455197.5 JD.

**Table 5.** Inferred parameters from substellar evolutionary models vs. measured parameters for the companion.

Property	TUCSON	ATMO2020	SM08 Hybrid	Measurement
Mass ( $M_{\text{Jup}}$ )	$75.0^{+5.3}_{-3.0}$ ( $1.5\sigma$ )	$69.8^{+5.6}_{-3.3}$ ( $2.8\sigma$ )	$66.1^{+8.1}_{-3.2}$ ( $3.9\sigma$ )	$81.9^{+5.8}_{-6.4}$
Age (Gyr)	$4.7^{+2.9}_{-2.1}$ ( $1.8\sigma$ )	$6.4^{+4.3}_{-3.1}$ ( $2.7\sigma$ )	$6.0^{+3.6}_{-2.4}$ ( $2.5\sigma$ )	$\geq 3.4$
$\log(L_{\text{bol}}/L_{\odot})$	$-4.57^{+0.08}_{-0.08}$ ( $0.03\sigma$ )	$-4.53^{+0.08}_{-0.08}$ ( $0.02\sigma$ )	$-4.48^{+0.07}_{-0.08}$ ( $0.2\sigma$ )	$-4.55 \pm 0.08$
$T_{\text{eff}}$ (K)	$1381 \pm 173$	$1413 \pm 177$	$1344 \pm 71$	–
$\log(g)$ ( $\text{cm s}^{-2}$ )	$5.30 \pm 0.02$	$5.43 \pm 0.02$	$5.34 \pm 0.06$	–
Radius ( $R_{\text{Jup}}$ )	$0.90 \pm 0.02$	$0.86 \pm 0.02$	$0.95 \pm 0.05$	–

NOTE: Masses were determined using measured  $\log(L_{\text{bol}})$  and age,  $\log(L_{\text{bol}})$  was derived from measured mass and age, and age was estimated from measured mass and  $\log(L_{\text{bol}})$ . Model-derived radii were based on the measured age and mass, while  $T_{\text{eff}}$  and  $\log g$  were determined using model radii and measured mass.

for cloud-free, later-type T dwarfs like Gl 229 B and Gl 758 B, and their effectiveness diminishes across the entire effective temperature range. On the other hand, the hybrid model does capture the transitional phase from L- to T-type cool brown dwarfs using the atmospheric model from Ackerman & Marley (2013) by varying the cloud sedimentation parameter. Particularly noteworthy is their discovery that the transition from cloudy L dwarfs to cloudless T dwarfs results in a deceleration of the evolutionary process, leading to an accumulation of substellar objects in the L/T transition phase. This finding is corroborated by several other recent studies such as Chen et al. (2022) who found evidence of slowed cooling on the L/T transition.

We use the method outlined in Dupuy et al. (2019) to infer masses of HD 63754 B based on its measured luminosity and age obtained from each evolutionary model. We adopt the broad age posterior in Figure 1 with a lower limit of 3.4 Gyr, and a luminosity of  $\log(L_{\text{bol}}/L_{\odot}) = -4.55 \pm 0.08$  dex as previously derived. Briefly, we use an importance sampling approach to calculate inferred masses for each evolutionary model drawing random samples from the distributions of bolometric luminosity and age. Then, we bilinearly interpolate the model grid to determine the companion's mass corresponding to the given age and luminosity values. We repeat the process to build a model-derived mass distribution from each model. The inferred mass distributions for the three evolutionary grids are depicted in Figure 6, along with our measured dynamical mass dis-

tribution of HD 63754 B from the orbital fit. In a similar fashion, we use this importance sampling technique to estimate the posterior distributions for age with known MCMC mass posterior and our inferred luminosity, and for luminosity with known masses and age.

We quantify the differences between the model-independent measurements of mass, age and luminosity ( $X_{\text{model-inferred}}$ ) and model-inferred masses ( $X_{\text{empirical}}$ ) by computing the probability  $P(X_{\text{model-inferred}} > X_{\text{empirical}})$ . The discrepancy in model-derived and model-independent values can be converted to a one-sided Gaussian-equivalent standard deviation via the special error function:

$$\sigma = \sqrt{2} \text{erf}^{-1}(1 - 2P(X_{\text{model-inferred}} > X_{\text{empirical}})) \quad (2)$$

We list the inferred parameters including mass, age, luminosity, effective temperature, radius and surface gravity extracted from different evolutionary models in Table 5.

Here, we compare the model-inferred parameters with empirically measured mass, age and luminosity of HD 63754 B. Figure 6 shows the model-independent and model-inferred histograms for mass, age and luminosity as sourced from the TUCSON, the ATMO 2020 and the SM08 hybrid models, respectively. The measured and inferred parameters are consistent within  $3\sigma$  except for the agreement between the hybrid model masses and the dynamical mass ( $4\sigma$ ). Figure 7 illustrates the position of HD 63754 B with respect to the predicted masses and ages from each of the three evolutionary models. The Burrows et al. (1997) TUCSON model emerges as the closest match

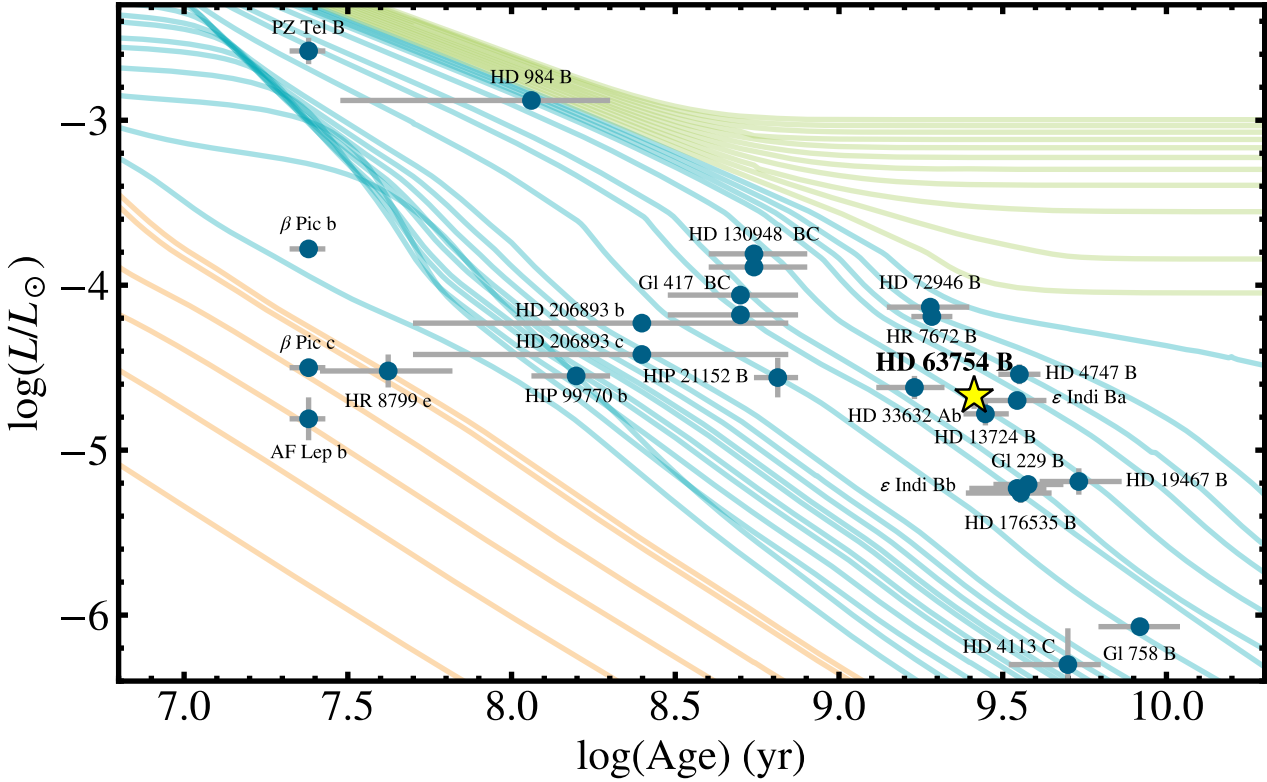


**Figure 8.** Imaged planets and brown dwarfs with dynamical masses, together with models of the luminosity evolution of planets (orange), brown dwarfs (blue), and low-mass stars (green) across various mass ranges [Burrows et al. \(1997\)](#). Our companion HD 63754 B is highlighted by the yellow star using the lower limit on the age of  $> 3.4$  Gyr and a dynamical mass of  $81.9^{+6.4}_{-5.8} M_{\text{Jup}}$ . The age uncertainty is not shown. Luminosity and age data for the majority of systems are tabulated in [Franson et al. \(2023\)](#) with additional systems noted in [\(Franson & Bowler 2023\)](#).

to our measured parameters for HD 63754 B, providing an inferred mass of  $75.0^{+5.3}_{-3.0} M_{\text{Jup}}$  about  $1.5\sigma$  away from our dynamical mass measurement given the measured age and luminosity. However, we note that this observed better agreement with the TUCSON grid is likely a coincidental outcome rather than indicative of a better fit. Several important caveats must be considered when interpreting these comparisons. First, the TUCSON evolutionary model grids are specifically calibrated for effective temperatures ranging from 125 to 1200 K, which are applicable only to T dwarfs and colder brown dwarfs. In contrast, the newer ATMO 2020 and SM08 hybrid models are more appropriate for L/T transition brown dwarfs like HD 63754 B, covering a broader effective temperature range of 700 to 2000 K. Furthermore, the cloudless TUCSON model being the best-fit model contradicts HD 63754 B's L/T transition spectral type determination. The slightly above-solar metallicity observed in HD 63754 B's host star also argues against a scenario of low opacity and a cloudless model, suggesting instead the presence of a cloudy atmosphere that could influence its thermal evolution.

Our measured and model-inferred parameters presented in Table 5, and by extension the comparison between them, could also be biased by additional sources of error. The spectral typing method employed here, which relies on color relations, is less accurate than empirical spectral fitting. This is exemplified by our recent work on HD 176535 B (HIP 93398 B) ([Li et al. 2023](#)), which was mistakenly classified as a T6 brown dwarf using single-band photometry but

was later revised to a late-L brown dwarf based on follow-up spectra ([Lewis et al. 2024, submitted](#)). Additionally, the dynamical mass of HD 63754 B exceeds the mass range of substellar models considered here (typically  $\leq 0.075 M_{\odot} \approx 78.6 M_{\text{Jup}}$ ), potentially introducing systematic uncertainties in the model-inferred parameters.

Figure 8 shows a comprehensive list of imaged brown dwarfs with independently measured age, mass and luminosity. The location of HD 63754 B is shown by the yellow star. While the majority of benchmark brown dwarfs with independent simultaneous age, mass, and luminosity measurements generally agree with evolutionary model predictions (e.g. HD 4747 B ([Peretti et al. 2019](#)), HD 33632 Ab ([Currie et al. 2021](#)), Gl 758 B ([Bowler et al. 2018](#))), a handful of brown dwarf systems bear pronounced discrepancies with evolutionary models. Previous statistical investigations ([Brandt et al. 2021a; Dupuy et al. 2019; Li et al. 2023; Franson et al. 2023](#)) on benchmark brown dwarfs underscore two emerging trends: 1) some measured brown dwarfs are over-luminous in their early stages of evolution 2) others are under-luminous at high masses and old ages, in tension with their observed spectral types.

The first trend, or the under-luminosity problem at young substellar ages, exemplified by HD 130948 BC ([Dupuy et al. 2009](#)), has been poorly explained. Most evolutionary models suggest that brown dwarfs could not have cooled to the observed luminosity at young ages. Similarly, their measured masses are unexpectedly low, or the ages of their host stars are older than the cooling ages of substellar

objects. Such under-massive systems include HD 13724 B ( $4\sigma$  age discrepancy) [Rickman et al. \(2020\)](#), HD 130948 BC ( $3\sigma$ ), Gl 417 BC ( $1\sigma$ ) ([Dupuy et al. 2014](#)), and CWW 89 Ab ( $7\sigma$ ). While a variety of mechanisms have been considered, including inhomogeneous dust clouds, non-equilibrium chemistry, thermal inversion, magnetic activity, non-solar metallicity, vertical mixing, and cloud formation, none have provided a comprehensive account of this phenomenon, although thermal inversion could partially explain the slowed cooling of specific L and T brown dwarfs like CWW 89 A ([Gagliuffi et al. 2014](#)). Atmospheric retrieval of L-type brown dwarfs has revealed upper atmospheric heating or similar surface processes ([Burningham et al. 2017](#)) may contribute partially to the over-luminosity problem, but the major causes are still unclear to date.

The latter trend, known as the over-luminosity brown dwarf problem, has several possible explanations. This problem is now evident in a significant number of brown dwarfs, including Gl 229 B ([Brandt et al. 2020](#)), HD 19467 B ([Maire et al. 2020](#)), HD 47127 B ([Bowler et al. 2021](#)), HD 176535 B ([Li et al. 2023](#)), and HD 4113 C ([Cheetham et al. 2018](#)). The first possible resolution for this discrepancy can be attributed to unresolved multiplicity in these brown dwarf systems. Multiplicity studies find a relatively high binary fraction of  $8\pm6\%$  for ultracool T8-Y0 brown dwarfs ([Fontanive et al. 2018](#)). The discrepancy may also arise from inherent inaccuracies in our orbit modeling using Hipparcos-Gaia proper motion anomaly, especially in the high sigma regime. More accurate solutions are expected with the upcoming Gaia DR4 release in 2025. We discuss this in more detail in section 6.3. If the over-massive issue cannot be ascribed to unresolved multiplicity or inaccuracies in astrometric data, it may indicate a deeper problem with the evolutionary models and their underlying assumptions. Rectifying this situation would likely require substantial overhauls in how these models handle fundamental properties such as the equation of state, thermal transport in the interior structure, or the effects of rotation and magnetism ([Marley et al. 2021](#)).

One of the earliest discovered and coolest brown dwarfs, Gl 229 B, is a significant outlier in this over-luminosity regime. Its mass and luminosity significantly differ from evolutionary model predictions. Neither low metallicity nor the presence of a massive, inner companion can address this discrepancy. The likely explanation based on multi-decade observations could be that Gl 229 B itself is an unresolved binary system ([Brandt et al. 2021a](#)) with a total system mass of  $71.4 M_{\text{Jup}}$ . Although the departure from evolutionary model predictions is not as severe as are the cases with Gl 229 B ( $10\sigma$ ) and HD 4113 C ( $5\sigma$ ), HD 63754 B still falls into this category with a discrepancy at levels as large as  $3\sigma$ , even at older ages. We list several possibilities for the extra mass in the HD 63754 AB system. 1) HD 63754 B has a low-mass-ratio binary companion, whose flux would contribute negligibly to the integrated spectrum or the infrared photometry of HD 63754 B. 2) There are additional companions in the HD 63754 AB system. We find no evidence of any wide, massive companions in our Keck/NIRC2 AO imaging as shown in Figure 3, but we cannot make the conclusion with a single night data over only about an hour integration time. Our orbital fit to the RV and absolute astrometric data in Figure 5 also cannot rule out disturbance to the system from a less massive, inner companion or a binary companion to HD 63754 B. The relative orbit has a high scatter and relies on only a single astrometry point which leaves some space for either an unresolved binary companion around HD 63754 B or additional exoplanets in the HD 63754 AB system. Further high-resolution imaging with smaller inner working angles and spectroscopic observations may identify any potential additional companions. 3) HD 63754 B

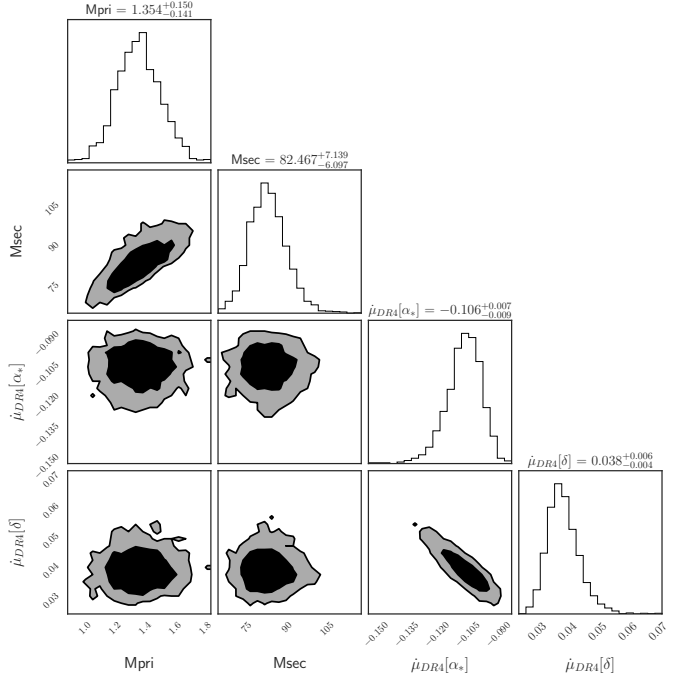


**Figure 9.** Corner plot showing the mass distribution of the HD 63754 AB system and the projected accelerations from the orbital fit at the Gaia DR4 central epoch of 2017.5. No strong correlations are seen between the companion mass and DR4 predicted accelerations based on current measurements, which means that DR4 may not be as useful in further constraining the dynamical mass of HD 63754 B.

is not an isolated incidence but rather an indication of a systematic problem with evolutionary models ([Brandt et al. 2021a](#)).

### 6.3 Predicted Accelerations for Gaia DR4

Gaia Data Release 4 (DR4), scheduled for release in 2025, will offer high-precision individual epoch astrometry and a 5-year time baseline, providing more precise constraints on planetary orbits. We forward-model HD 63754 A's predicted stellar accelerations at Gaia DR4's central epoch of 2017.5 using projections from our MCMC `orvara` result for HD 63754 B. We employ an adaptation of the epoch astrometry fitting code `htof` ([Brandt et al. 2021b](#)), which is an open-source tool to fit arbitrary high-order astrometric solutions to epoch astrometry. The predicted astrometric acceleration caused by HD 63754 B at 2017.5 is  $\dot{\mu}_{DR4,\alpha_*} = -0.106^{+0.007}_{-0.009} \text{ m/s/yr}$  and  $\dot{\mu}_{DR4,\delta} = 0.038^{+0.006}_{-0.004} \text{ m/s/yr}$ , with the uncertainty coming from the range of orbits compatible with existing data. Figure 9 shows a corner plot of the masses of the two known bodies in the HD 63754 system and their correlation with the predicted Gaia DR4 accelerations. The correlation coefficients between DR4 accelerations and the mass of HD 63754 B are close to zero, suggesting that Gaia DR4 may not be as useful in refining HD 63754 B's dynamical mass and validating our orbital solution. This is unsurprising given the large separation of this massive companion. Gaia DR4 will be sensitive to short period companions which will be useful if they can also be found with speckle imaging. For now, whether there are additional companions in the HD 63754 AB system remains unresolved. Further RV, direct imaging and spectroscopic monitoring will clarify the nature of this system.

## 7 CONCLUSION

In this study, we presented the joint astrometric and direct imaging discovery of HD 63754 B, a companion selected for observation in our Keck-HGCA accelerating stars program because of its significant *Hipparcos-Gaia* astrometric signature. We carried out comprehensive orbital and evolution modeling using empirical measurements of stellar velocities, activity-age indicators, direct imaging photometry, and evolutionary theoretical isochrones. The derived dynamical mass for HD 63754 B is  $81.9^{+6.4}_{-5.8} M_{\text{Jup}}$ , with an inferred activity age  $>3.4$  Gyr and a bolometric luminosity of  $\log(L_{\text{bol}}/L_{\odot}) = -4.55 \pm 0.08$  dex. Comparison of our findings regarding dynamical mass, age, and luminosity with substellar evolutionary models reveals that HD 63754 B exhibits characteristics of being over-massive and under-luminous relative to model-predicted outcomes. We conclude that such discrepancies could stem from uncertainties in stellar age determination, potential systematic biases in evolutionary models, or unresolved multiplicity within the system.

HD 63754 B, alongside several other objects, poses a challenge to the current understanding of substellar cooling models. While the precise nature of HD 63754 B remains unclear, its L' band photometry provides support for a substellar classification, particularly favoring a brown dwarf on the L/T transition. We anticipate that additional orbital or spectroscopic measurements will finally clarify the nature of HD 63754 B. Enhanced observational data for a broader sample of brown dwarfs discovered through acceleration could significantly refine our comprehension of the substellar evolution paradigm.

## 8 ACKNOWLEDGEMENT

This research utilized data from the Keck Observatory Archive (KOA), operated jointly by the W. M. Keck Observatory and the NASA Exoplanet Science Institute (NExSci), under contract with the National Aeronautics and Space Administration (NASA). The findings presented herein made use of data from the European Space Agency (ESA) Gaia space mission, with data processing conducted by the Gaia Data Processing and Analysis Consortium (DPAC). Financial support for the DPAC is provided by national institutions, particularly those institutions participating in the Gaia MultiLateral Agreement (MLA). The Gaia mission website is <https://www.cosmos.esa.int/gaia> and the Gaia archive can be accessed at <https://archives.esac.esa.int/gaia>. T.D.B. gratefully acknowledges support from the Alfred P. Sloan Foundation and from the NASA Exoplanet Research Program under grant #80NSSC18K0439. B.L.L. acknowledges support from the National Science Foundation Graduate Research Fellowship under Grant No. 2021-25 DGE-2034835. Any opinions, findings, and conclusions or recommendations expressed in this material are those of the authors(s) and do not necessarily reflect the views of the National Science Foundation. B.P.B. acknowledges support from the NASA Exoplanet Research Program grant 20-XRP20\_2-0119 and the Alfred P. Sloan Foundation. R.K. acknowledges the support by the National Science Foundation under Grant No. NSF PHY-1748958. We thank the Heising Simons Foundation for their support.

## DATA AVAILABILITY

This manuscript includes data acquired by the NIRC2 camera at the W. M. Keck Observatory (WMKO), accessible to the public via the Keck Observatory Archive (KOA), which is jointly managed by the WMKO and NASA Exoplanet Science Institute (NExSci). This

research is funded by the National Aeronautics and Space Administration. All data in this paper are publicly available in the KOA. The data are analyzed with the orvara and VIP open-source packages, which are publicly available at <https://github.com/t-brandt/orvara> and <https://github.com/vortex-exoplanet/VIP>, respectively. We also acknowledge the use of public Gaia EDR3 data through the Gaia Archive at <https://gea.esac.esa.int/archive/>.

## REFERENCES

- Ackerman, A. S., & Marley, M. S. 2013, The Astrophysical Journal, 765, 75
- Aguilera-Gómez, C., Ramírez, I., & Chanamé, J. 2018, A&A, 614, A55
- Allard, F., Homeier, D., & Freytag, B. 2012, Philosophical Transactions of the Royal Society of London Series A, 370, 2765
- Amara, A., & Quanz, S. P. 2012, MNRAS, 427, 948
- Anders, F., Khalatyan, A., Chiappini, C., et al. 2019, A&A, 628, A94
- André, P., Basu, S., & Inutsuka, S. 2009, in Structure Formation in Astrophysics, ed. G. Chabrier (Cambridge University Press), 254
- Balfour, S. K., Whitworth, A. P., Hubber, D. A., & Jaffa, S. E. 2015, MNRAS, 453, 2471
- Baraffe, I., Chabrier, G., Barman, T. S., Allard, F., & Hauschildt, P. H. 2003, A&A, 402, 701
- Baraffe, I., Homeier, D., Allard, F., & Chabrier, G. 2015, A&A, 577, A42
- Beichman, C., Gelino, C. R., Kirkpatrick, J. D., et al. 2013, ApJ, 764, 101
- Bessell, M. S., & Brett, J. M. 1988, PASP, 100, 1134
- Bochanski, J. J., Faherty, J. K., Gagné, J., et al. 2018, AJ, 155, 149
- Bonavita, M., Fontanive, C., Gratton, R., et al. 2022, Monthly Notices of the Royal Astronomical Society, 513, 5588
- Bowler, B. P. 2016, PASP, 128, 102001
- Bowler, B. P., Blunt, S. C., & Nielsen, E. L. 2020, AJ, 159, 63
- Bowler, B. P., Cochran, W. D., Endl, M., et al. 2021, AJ, 161, 106
- Bowler, B. P., Dupuy, T. J., Endl, M., et al. 2018, AJ, 155, 159
- Bowler, B. P., Tran, Q. H., Zhang, Z., et al. 2023, AJ, 165, 164
- Brandt, G. M., Dupuy, T. J., Li, Y., et al. 2021a, AJ, 162, 301
- Brandt, G. M., Michalik, D., Brandt, T. D., et al. 2021b, AJ, 162, 230
- Brandt, T. D. 2018, ApJS, 239, 31
- Brandt, T. D. 2021, ApJS, 254, 42
- Brandt, T. D., Dupuy, T. J., & Bowler, B. P. 2019, The Astrophysical Journal, 871, 63
- Brandt, T. D., Dupuy, T. J., Bowler, B. P., et al. 2020, The Astronomical Journal, 160, 196
- Brandt, T. D., Dupuy, T. J., Li, Y., et al. 2021c, AJ, 162, 186
- Brandt, T. D., Kuzuhara, M., McElwain, M. W., et al. 2014, ApJ, 786, 1
- Bressan, A., Marigo, P., Girardi, L., et al. 2012, MNRAS, 427, 127
- Brewer, J. M., Fischer, D. A., Valenti, J. A., & Piskunov, N. 2016, ApJS, 225, 32
- Burningham, B., Marley, M. S., Line, M. R., et al. 2017, MNRAS, 470, 1177
- Burns, A., Marley, M., Hubbard, W. B., et al. 1997, ApJ, 491, 856
- Chabrier, G., Baraffe, I., Allard, F., & Hauschildt, P. 2000, The Astrophysical Journal, 542, 464
- Chabrier, G., Baraffe, I., Allard, F., & Hauschildt, P. H. 2005, arXiv e-prints, astro
- Chabrier, G., Baraffe, I., Phillips, M., & Debras, F. 2023, A&A, 671, A119
- Cheetham, A., Ségransan, D., Peretti, S., et al. 2018, A&A, 614, A16
- Chen, M., Li, Y., Brandt, T. D., et al. 2022, AJ, 163, 288
- Christiaens, D., Cordero-Grande, L., Pietsch, M., et al. 2021, NeuroImage, 225, 117437
- Costa Silva, A. R., Delgado Mena, E., & Tsantaki, M. 2020, A&A, 634, A136
- Crepp, J. R., & Johnson, J. A. 2014, Research in Astronomy and Astrophysics, 14, 887
- Crepp, J. R., Johnson, J. A., Howard, A. W., et al. 2014, The Astrophysical Journal, 781, 16
- Currie, T., Brandt, G. M., Brandt, T. D., et al. 2023, Science, 380, 198
- Currie, T., Brandt, T. D., Kuzuhara, M., et al. 2021, in Society of Photo-Optical Instrumentation Engineers (SPIE) Conference Series, Vol. 11823,

- Techniques and Instrumentation for Detection of Exoplanets X, ed. S. B. Shaklan & G. J. Ruane, 1182304
- Cutri, R. M., Skrutskie, M. F., van Dyk, S., et al. 2003, VizieR Online Data Catalog, II/246
- Cutri, R. M., Wright, E. L., Conrow, T., et al. 2021, VizieR Online Data Catalog, II/328
- Delgado Mena, E., Bertrán de Lis, S., Adibekyan, V. Z., et al. 2015, *A&A*, 576, A69
- Delgado Mena, E., Moya, A., Adibekyan, V., et al. 2019, *A&A*, 624, A78
- Dieterich, S. B., Henry, T. J., Jao, W.-C., et al. 2014, *AJ*, 147, 94
- Dobbs, C. 2013, *Astronomy & Geophysics*, 54, 5.24
- Duncan, D. K., Vaughan, A. H., Wilson, O. C., et al. 1991, *ApJS*, 76, 383
- Dupuy, T. J., Kratter, K. M., Hinkley, S., et al. 2019, *The Astrophysical Journal*, 874, 29
- Dupuy, T. J., & Liu, M. C. 2017, *The Astrophysical Journal Supplement Series*, 231, 15
- Dupuy, T. J., Liu, M. C., & Ireland, M. J. 2009, *The Astrophysical Journal*, 692, 729
- Dupuy, T. J., Liu, M. C., & Ireland, M. J. 2014, *The Astrophysical Journal*, 790, 133
- ESA, ed. 1997, ESA Special Publication, Vol. 1200, The HIPPARCOS and TYCHO catalogues. Astrometric and photometric star catalogues derived from the ESA HIPPARCOS Space Astrometry Mission
- Filippazzo, J. C., Rice, E. L., Faherty, J., et al. 2015, *ApJ*, 810, 158
- Fontanive, C., Biller, B., Bonavita, M., & Allers, K. 2018, *MNRAS*, 479, 2702
- Fontanive, C., Mužić, K., Bonavita, M., & Biller, B. 2019, *MNRAS*, 490, 1120
- Forbes, J. C., & Loeb, A. 2019, *ApJ*, 871, 227
- Foreman-Mackey, D., Hogg, D. W., Lang, D., & Goodman, J. 2013, *PASP*, 125, 306
- Franson, K., & Bowler, B. P. 2023, *AJ*, 165, 246
- Franson, K., Bowler, B. P., Bonavita, M., et al. 2022, arXiv e-prints, arXiv:2211.09840
- Franson, K., Bowler, B. P., Bonavita, M., et al. 2023, *The Astronomical Journal*, 165, 39
- Gagliuffi, D. C. B., Burgasser, A. J., Gelino, C. R., et al. 2014, *The Astrophysical Journal*, 794, 143
- Gaia Collaboration. 2020, VizieR Online Data Catalog, I/350
- Gaia Collaboration. 2022, VizieR Online Data Catalog, I/355
- Gomes da Silva, J., Santos, N. C., Adibekyan, V., et al. 2021, *A&A*, 646, A77
- Gomez Gonzalez, C. A., Wertz, O., Absil, O., et al. 2017, *AJ*, 154, 7
- Gonzales, E. C. 2020, in American Astronomical Society Meeting Abstracts, Vol. 235, American Astronomical Society Meeting Abstracts #235, 132.04
- Hallakoun, N., Maoz, D., Istrate, A. G., et al. 2023, *Nature Astronomy*, 2306.08672
- Henriksen, R. N. 1986, *ApJ*, 310, 189
- Hester, J. J., Scowen, P. A., Sankrit, R., et al. 1996, *AJ*, 111, 2349
- Høg, E., Fabricius, C., Makarov, V. V., et al. 2000, *A&A*, 355, L27
- Holmberg, J., Nordström, B., & Andersen, J. 2009, *A&A*, 501, 941
- Huby, E., Baudoz, P., Mawet, D., & Absil, O. 2015, *A&A*, 584, A74
- Huby, E., Bottom, M., Femenia, B., et al. 2017, *A&A*, 600, A46
- Kirkpatrick, J. D., Reid, I. N., Liebert, J., et al. 2000, *AJ*, 120, 447
- Kopytova, T. G., Brandner, W., Tognelli, E., et al. 2016, *A&A*, 585, A7
- Lafrenière, D., Marois, C., Doyon, R., Nadeau, D., & Artigau, É. 2007, *ApJ*, 660, 770
- Lagrange, A. M., Bonnefoy, M., Chauvin, G., et al. 2010, *Science*, 329, 57
- Leggett, S. K., Allard, F., & Hauschildt, P. H. 1998, *ApJ*, 509, 836
- Levine, J. L., Steinhauer, A., Elston, R. J., & Lada, E. A. 2006, *ApJ*, 646, 1215
- Li, Y., Brandt, T. D., Brandt, G. M., et al. 2023, arXiv e-prints, arXiv:2301.10420
- Li, Y., Brandt, T. D., Brandt, G. M., et al. 2021, *AJ*, 162, 266
- Liu, M. C., Fischer, D. A., Graham, J. R., et al. 2002, *ApJ*, 571, 519
- Llorente de Andrés, F., Chavero, C., de la Reza, R., Roca-Fabrega, S., & Cifuentes, C. 2021, *A&A*, 654, A137
- Lodders, K., & Fegley, B. 2002, *Icarus*, 155, 393
- Luck, R. E. 2017, *AJ*, 153, 21
- Lunine, J. I., Hubbard, W. B., & Marley, M. S. 1986, *ApJ*, 310, 238
- Maire, A. L., Molaverdikhani, K., Desidera, S., et al. 2020, *A&A*, 639, A47
- Mamajek, E. E., & Hillenbrand, L. A. 2008, *The Astrophysical Journal*, 687, 1264
- Marley, M. S., Saumon, D., Visscher, C., et al. 2021, *ApJ*, 920, 85
- Marois, C., Macintosh, B., & Véran, J.-P. 2010, in *Adaptive Optics Systems II*, ed. B. L. Ellerbroek, M. Hart, N. Hubin, & P. L. Wizinowich, Vol. 7736 (SPIE), 77361J
- Marsakov, V. A., & Shevlev, Y. G. 1995, *Bulletin d'Information du Centre de Données Stellaires*, 47, 13
- Mawet, D., Milli, J., Wahhaj, Z., et al. 2014, *ApJ*, 792, 97
- McKee, C. F., & Ostriker, E. C. 2007, *ARA&A*, 45, 565
- Murgas, F., Jenkins, J. S., Rojo, P., Jones, H. R. A., & Pinfield, D. J. 2013, *A&A*, 552, A27
- Nagpal, V., Blunt, S., Bowler, B. P., et al. 2023, *AJ*, 165, 32
- Nelder, J. A., & Mead, R. 1965, *The Computer Journal*, 7, 308
- Nielsen, E. L., De Rosa, R. J., Macintosh, B., et al. 2019, *AJ*, 158, 13
- Nony, T., Galván-Madrid, R., Motte, F., et al. 2023, *A&A*, 674, A75
- Pace, G. 2013, *A&A*, 551, L8
- Padoan, P., & Nordlund, Å. 2002, *ApJ*, 576, 870
- Padoan, P., & Nordlund, Å. 2004, *ApJ*, 617, 559
- Pägert, M., Mugrauer, M., Riffeser, A., et al. 2021, *Astronomy & Astrophysics*, 652, a58
- Pairet, B., Cantalloube, F., Gomez Gonzalez, C. A., Absil, O., & Jacques, L. 2019, *MNRAS*, 487, 2262
- Palla, M., Santos-Peral, P., Recio-Blanco, A., & Matteucci, F. 2022, *A&A*, 663, A125
- Peretti, S., Ségransan, D., Lavie, B., et al. 2019, *A&A*, 631, A107
- Peretto, N., Fuller, G. A., Duarte-Cabral, A., et al. 2013, *A&A*, 555, A112
- Phillips, T. G., Baraffe, I., Aigrain, S., & Mayne, N. J. 2020, *Astronomy & Astrophysics*, 637, A58
- Pinochet, J. 2019, *Physics Education*, 54, 055021
- Reipurth, B., & Clarke, C. 2001, *AJ*, 122, 432
- Rickman, E. L., Matthews, E., Ceva, W., et al. 2022, *A&A*, 668, A140
- Rickman, E. L., Ségransan, D., Hagelberg, J., et al. 2020, *A&A*, 635, A203
- Rickman, E. L., Ségransan, D., Marmier, M., et al. 2019, *A&A*, 625, A71
- Saumon, D., Marley, M., Abel, M., & Frommhold, L. 2008, *The Astrophysical Journal Supplement Series*, 178, 585
- Schneider, N., Csengeri, T., Klessen, R. S., et al. 2015, *A&A*, 578, A29
- Serabyn, E., Huby, E., Matthews, K., et al. 2017, *AJ*, 153, 43
- Service, M., Lu, J. R., Campbell, R., et al. 2016, *PASP*, 128, 095004
- Soubiran, C., Brouillet, N., & Casamiquela, L. 2022, *A&A*, 663, A4
- Soubiran, C., Jasniewicz, G., Chemin, L., et al. 2018, *A&A*, 616, A7
- Soubiran, C., Le Campion, J.-F., Brouillet, N., & Chemin, L. 2016, *A&A*, 591, A118
- Soummer, R., Pueyo, L., & Larkin, J. 2012, *The Astrophysical Journal*, 755, L28
- Stanford-Moore, S. A., Nielsen, E. L., De Rosa, R. J., Macintosh, B., & Czekala, I. 2020, *ApJ*, 898, 27
- Takeda, G., Ford, E. B., Sills, A., et al. 2007, *ApJS*, 168, 297
- Trifonov, T., Tal-Or, L., Zechmeister, M., et al. 2020, *A&A*, 636, A74
- Valenti, J. A., & Fischer, D. A. 2005, *ApJS*, 159, 141
- van Dokkum, P. G. 2001, *PASP*, 113, 1420
- Vaughan, A. H., & Preston, G. W. 1980, *Publications of the Astronomical Society of the Pacific*, 92, 385
- Voges, W., Aschenbach, B., Boller, T., et al. 1999, *A&A*, 349, 389
- Vogt, S. S., & Keane, M. J. 1993, in American Astronomical Society Meeting Abstracts, Vol. 183, American Astronomical Society Meeting Abstracts, 11.01
- Vousden, W. D., Farr, W. M., & Mandel, I. 2015, *Monthly Notices of the Royal Astronomical Society*, 455, 1919
- Wertz, O., Absil, O., Gómez González, C. A., et al. 2017, *A&A*, 598, A83
- Whitworth, A. 2018, arXiv e-prints, arXiv:1811.06833
- Wright, J. T., Marcy, G. W., Butler, R. P., & Vogt, S. S. 2004, *ApJS*, 152, 261
- Yee, S. W., Petigura, E. A., & von Braun, K. 2017, *ApJ*, 836, 77

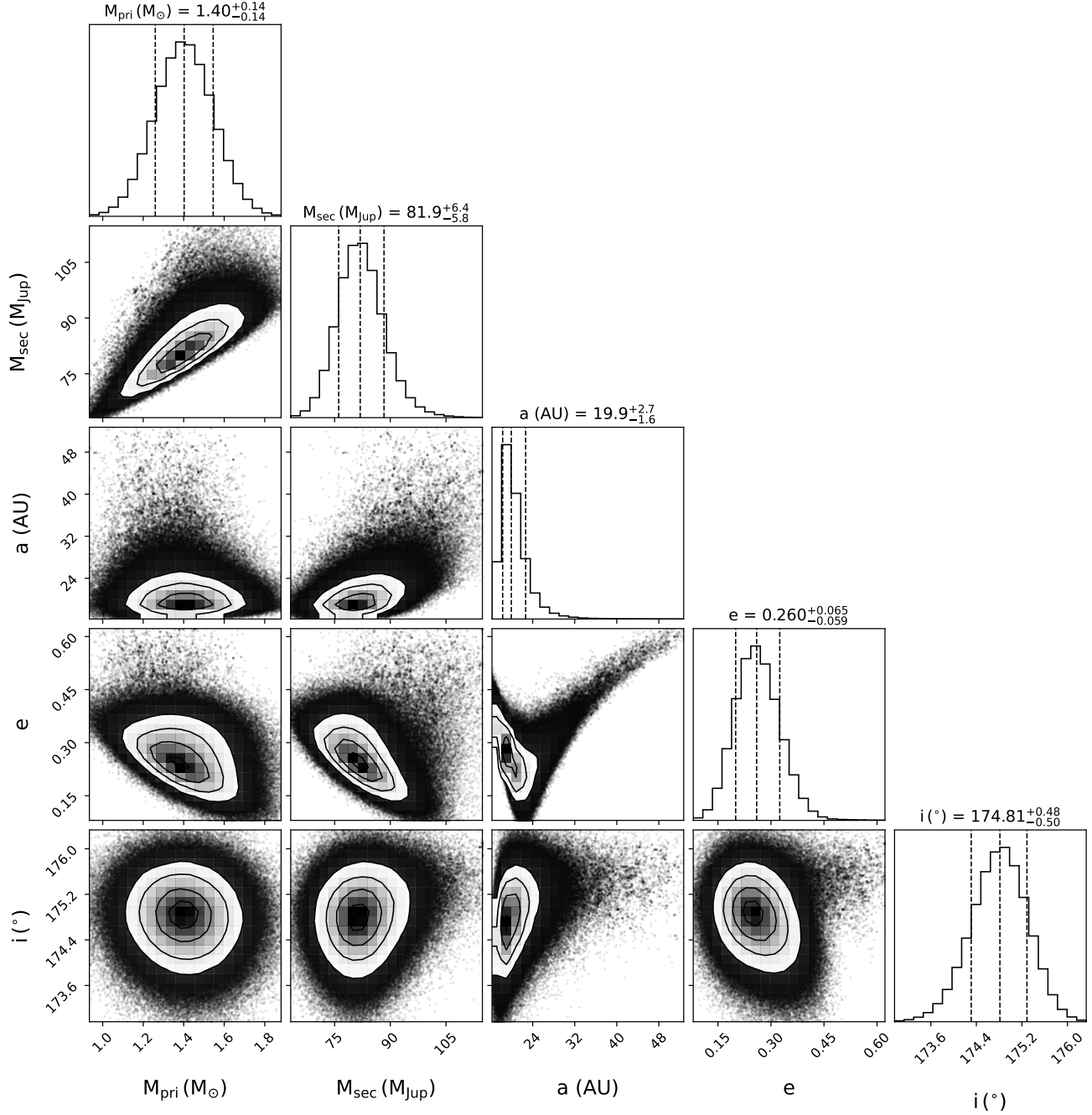


**Figure 10.** Posterior distributions using a Gaussian prior of  $1.41 \pm 0.15 M_{\odot}$  on the primary mass, both 1D and 2D, are presented for various orbital parameters of HD 63754 B. These distributions are derived from the analysis of radial velocity from HIRES and HARPS, relative astrometry obtained through Keck/NIRC2 direct imaging, and absolute astrometry from Hipparcos and Gaia data using `orvara` (Brandt et al. 2021c). The 1D posterior distributions are accompanied by confidence intervals at 15.85%, 50.0%, and 84.15%, with the median  $\pm 1\sigma$  values indicated. Additionally, the 2D posterior distribution is visualized with contour levels corresponding to 1, 2, and  $3\sigma$ .

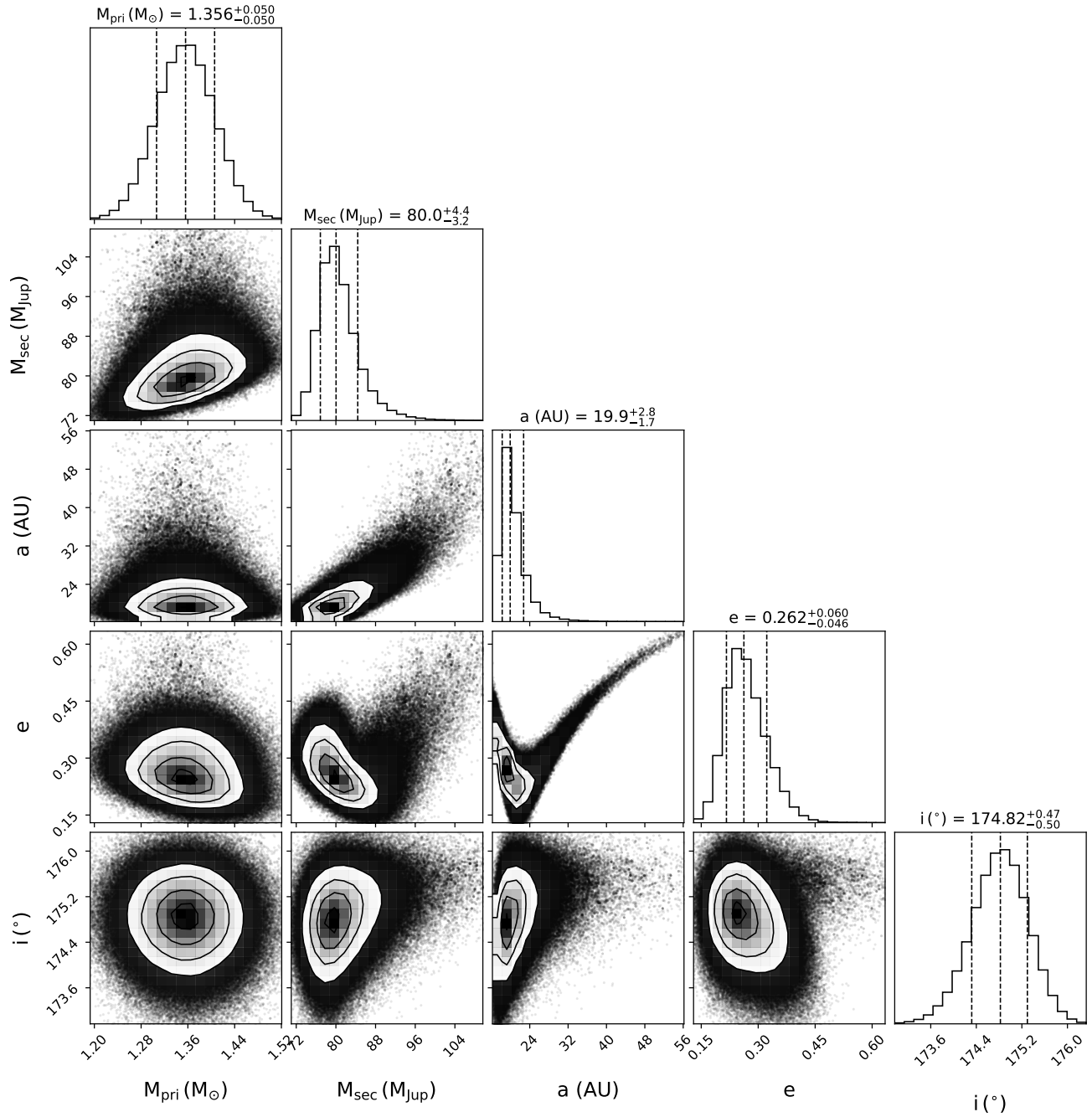


**Figure 11.** Same as Figure 10 but using a narrower Gaussian prior of  $1.41 \pm 0.05 M_{\odot}$  on the primary mass in the MCMC orbital modeling.